THE UNIVERSITY OF CHICAGO

DETECTING GRAVITATIONAL LENSING OF THE COSMIC MICROWAVE BACKGROUND BY GALAXY CLUSTERS

A DISSERTATION SUBMITTED TO
THE FACULTY OF THE DIVISION OF THE PHYSICAL SCIENCES
IN CANDIDACY FOR THE DEGREE OF
DOCTOR OF PHILOSOPHY

DEPARTMENT OF ASTRONOMY AND ASTROPHYSICS

BY

ERIC JONES BAXTER

CHICAGO, ILLINOIS

AUGUST 2014

TABLE OF CONTENTS

LIST OF FIGURES

ACKNOWLEDGMENTS

I thank my advisor Prof. Scott Dodelson for his support and guidance throughout my graduate career. I am especially grateful that he agreed to support me for an additional year, allowing me to find a postdoctoral position that I am excited about.

I thank Ryan Keisler and other members of the South Pole Telescope collaboration for their guidance on this project.

I thanks my committee members Profs. Dan Hooper, Andrey Kravtsov, and Stephan Meyer for their support and for their flexibility in scheduling my defense at last minute.

ABSTRACT

Clusters of galaxies gravitationally lens the Cosmic Microwave Background (CMB) leading to a distinct signal in the CMB on arcminute scales. Measurement of the cluster lensing effect offers the exciting possibility of constraining the masses of galaxy clusters using CMB data alone. Improved constraints on cluster masses are in turn essential to the use of clusters as cosmological probes: uncertainties in cluster masses are currently the dominant systematic affecting cluster abundance constraints on cosmology. To date, however, the CMB cluster lensing signal remains undetected because of its small magnitude and angular size. In this thesis, we develop a maximum likelihood approach to extracting the signal from CMB temperature data. We validate the technique by applying it to mock data designed to replicate as closely as possible real data from the South Pole Telescope's (SPT) Sunyaev-Zel'dovich (SZ) survey: the effects of the SPT beam, transfer function, instrumental noise and cluster selection are incorporated. We consider the effects of foreground emission on the analysis and show that uncertainty in amount of foreground lensing results in a small systematic error on the lensing constraints. Additionally, we show that if unaccounted for, the SZ effect leads to unacceptably large biases on the lensing constraints and develop an approach for removing SZ contamination. The results of the mock analysis presented here suggest that a 4σ first detection of the cluster lensing effect can be achieved with current SPT-SZ data.

INTRODUCTION

Cosmic Microwave Background (CMB) photons interact with the matter that fills our Universe as they make the journey from the last scattering surface to our detectors. These interactions can induce subtle distortions to the observed pattern of fluctuations in the CMB. While such distortions may be considered obstacles to the measurement of the primordial CMB, these secondary anisotropies can also be used as tools to probe the matter responsible for the distortions. Early work on distortions to the CMB induced by gravitational lensing suggested that measurement of this effect could be used to study galaxy formation [Blanchard and Schneider, 1987]. Subsequent analysis has shown that gravitational lensing allows the CMB to be used as a probe of large scale structure (LSS), enhancing the ability of CMB-only measurements to constrain e.g. the neutrino mass [Kaplinghat et al., 2003] and the properties of dark energy [Seljak and Zaldarriaga, 1999, Acquaviva and Baccigalupi, 2006]. In recent years, CMB experiments have achieved the necessary sensitivity to measure distortions caused by gravitational lensing [e.g. Smith et al., 2007, Dunkley et al., 2011, Keisler et al., 2011, Das et al., 2011, van Engelen et al., 2012, Planck Collaboration et al., 2013c]. To date, all measurements of gravitational lensing of the CMB have been related to lensing caused by LSS.

Clusters of galaxies – the most massive gravitationally bound structures in the Universe – are also expected to gravitationally lens the CMB. While the physical and mathematical descriptions of lensing of the CMB by galaxy clusters is largely identical to that of lensing by LSS, the distinction between the two different regimes is important. CMB cluster lensing is caused by *individual objects* rather than by LSS, and to date has *not* been detected. As pointed out by Seljak and Zaldarriaga [2000], CMB cluster lensing leads to a distinctive signal in the CMB in the vicinity (within tens of arcminutes) of galaxy clusters. The magnitude of this signal (roughly ten μK at peak) is near or below the current sensitivities of CMB telescopes, a fact that makes detection around individual clusters difficult. As we will see, though, it should be possible to detect this signal with current data by stacking constraints

from many clusters. The low noise levels of upcoming CMB experiments promise to make constraints on the CMB cluster lensing signal much tighter, and to make measurement of the signal for individual clusters an exciting and realistic possibility.

The CMB cluster lensing signal is a potentially powerful probe of the masses of galaxy clusters [e.g. Seljak and Zaldarriaga, 2000, Dodelson, 2004a, Holder and Kosowsky, 2004, Vale et al., 2004, Hu et al., 2007a]. Because lensing is sensitive only to mass, measurement of CMB cluster lensing does not depend on the details of complicated cluster physics. Other observables used to measure cluster masses – such as the Sunyaev-Zel'dovich Effect (SZE), galaxy counts (richness) and X-ray temperature – are only indirectly sensitive to the cluster mass. The use of these observables as proxies for mass requires the calibration of mass-observable relations, which may have large systematic uncertainties owing to our incomplete understanding of e.g. galaxy formation and cluster gas physics. Consequently, even if a CMB experiment is not sensitive enough to measure the CMB cluster lensing signal for a single cluster, measurement of the combined (stacked) effect from many clusters is still very useful because it can be used to tighten the error bars on mass-observable relationships. This is a particularly exciting possibility for CMB surveys attempting to find clusters via the SZE. Currently, such surveys must rely on external data sets (such as X-ray) to calibrate the relationship between the SZE-observable and the cluster mass. With CMB cluster lensing measurements, the same data that is used to measure the SZE can be used to constrain the cluster mass.

Improvements in cluster mass constraints are essential to extracting the maximum amount of cosmological information from cluster observations. The cluster abundance per comoving volume element, dN/dV, is sensitive to the growth of structure (through dN) as well as the expansion history of the Universe (through dV). This dual sensitivity means that cluster abundance measurements are uniquely qualified to distinguish between dark energy models and modified gravity [Huterer et al., 2013]. Assuming General Relativity and a Dark Energy model, measurement of the expansion history of the Universe determines the growth rate;

measurement of the growth rate can then be used as a test of General Relativity vs. modified gravity. Measurement of the expansion history alone is insufficient to distinguish between dark energy and modified gravity because dark energy models can generally be tuned to reproduce any expansion history predicted by a modified gravity model [e.g. Koyama and Maartens, 2006].

In order to extract constraints on a cosmological model from cluster abundance measurements, one must use the model to make a prediction for the cluster abundance as a function of mass and redshift. However, because clusters are extremely massive objects that live at the tails of an exponentially falling mass function, these abundance predictions are highly sensitive to cluster masses. As a result, uncertainties in cluster masses are currently the dominant systematic affecting cluster abundance constraints on cosmology [e.g. Rozo et al., 2010]. With reduced mass uncertainties, clusters can potentially be used to place tighter constraints on the properties of dark energy and modified gravity than any other probe of large scale structure [Albrecht et al., 2006].

Recent results from the Planck satellite highlight the importance of accurately estimating cluster masses. Cosmological constraints derived from the Planck team's measured CMB temperature power spectrum [Planck Collaboration et al., 2013a] are in tension with cosmological constraints derived from Planck team's measurement of the abundance of clusters detected via the SZE [Planck Collaboration et al., 2013b]. Planck detected fewer clusters via the SZE than would be expected based on the cosmological parameters derived from their measurement of the primary CMB anisotropy. One possible resolution to this tension is the introduction of massive neutrinos into the cosmological model; neutrinos tend to wash out structure and would therefore reduce the predicted number of clusters [Planck Collaboration et al., 2013b]. However, the tension can also be resolved by allowing for systematic uncertainty in the relation between SZE- and X-ray-derived cluster masses [Planck Collaboration et al., 2013b]. Resolving the apparent tension (and potentially measuring the masses of neutrinos) therefore requires better calibration of cluster mass-observable relations.

CMB cluster lensing also offers several important advantages over other measures of weak gravitational lensing around clusters. Traditional probes of weak lensing by clusters rely on measuring the gravitational distortion of galaxy shapes in the vicinity of clusters [see Hoekstra and Jain, 2008, for a review]. While these measurements have been conducted with much success, they also have significant limitations. For one, measuring the shapes of galaxies at high redshift is difficult, which in turn makes obtaining masses for high redshift clusters difficult. The CMB cluster lensing signal, on the other hand, is relatively insensitive to redshift. Galaxy distortion measurements are also affected by several sources of systematic error. For example, the redshifts of distorted galaxies are often determined photometrically; incomplete understanding of the photometric redshift error distribution can lead to biased cluster masses [Ma et al., 2006]. Additionally, galaxies can be be preferentially oriented along certain directions as a result of the galaxies living in the tidal field of some larger structure. These so-called intrinsic alignments can again result in biased cluster mass constraints [e.g. Croft and Metzler, 2000]. CMB cluster lensing is largely complementary to weak lensing shear measurements because it does not suffer from these sources of systematic error. Of course, CMB cluster lensing has its own associated systematics, as discussed in more detail below.

The above discussion is somewhat premature as the CMB cluster lensing signal has yet to be detected. It is unlikely that a first detection of the effect will have significant power to place cosmologically useful constraints on cluster masses. Furthermore, it may be the case that for low redshift clusters, CMB cluster lensing constraints on cluster masses will never be tighter than constraints based on measurement of galaxy lensing. Only at high redshift ($z \gtrsim 1$) will future CMB experiments begin to be competitive with other probes of weak lensing [e.g. Lewis and King, 2006]. At this point in time, we view measurement of the CMB cluster lensing as worthwhile simply because it has never been observed before. In the future, measurement of CMB cluster lensing will allow for improved understanding of weak lensing systematics and will generate cosmologically useful constraints on cluster masses.

Additionally, if both CMB lensing and galaxy lensing measurements can be attained around individual clusters, one can measure cosmographic distance ratios which in turn can be used to constrain cosmological parameters [Hu et al., 2007b].

The CMB cluster lensing signal is on the order of several μK and extends over several arcminutes; detecting this signal requires a low noise CMB experiment with fine angular resolution. Large survey area is also desirable as it means that more clusters are detected. Of the currently operating CMB telescopes, the South Pole Telescope is perhaps best qualified to make a first detection of the CMB cluster lensing signal. The SPT has recently completed the 4 year long SPT-SZ survey with the aim of constraining cosmology and detecting galaxy clusters via the SZE. The high angular resolution (roughly 1 arcminute), low noise levels (roughly 18 μK-arcmin at 150 GHz), and large sky coverage (2500 sq. deg.) achieved over the course of the SPT-SZ survey make this dataset well suited to detecting the cluster lensing effect. For this reason, we have tailored our discussion to data from SPT.

The goal of this thesis is to present a methodology for obtaining a first detection of the CMB cluster lensing signal and to make realistic projections for the strength of the detection that can be obtained with data from the SPT and future CMB experiments. We develop a maximum likelihood approach to constraining the lensing signal for a single cluster and for combining constraints from multiple clusters. By generating and analyzing mock data, we establish that the approach developed here is robust and we constrain the levels of expected systematics. While previous work [e.g. Dodelson, 2004a, Holder and Kosowsky, 2004, Vale et al., 2004, Lewis and King, 2006, Hu et al., 2007a] has explored the potential for constraining cluster masses using the CMB cluster lensing effect, the projections made therein have relied on a Fisher matrix approach or highly idealized data. Here, we significantly extend the accuracy of projections by generating and analyzing highly realistic mock data. To that end, we use a realistic cluster catalog and apply instrumental noise models, beam and transfer functions, and pixelization that are taken directly from SPT data. We consider a practical approach to eliminating SZ contamination, and study the effects of lensed and unlensed

foreground emission on the CMB cluster lensing constraints. One of our primary results is to show that with current data from the SPT-SZ survey we should be able to detect the cluster lensing effect at $\sim 4\sigma$ significance.

The thesis is organized as follows. In §1 we provide the necessary background for understanding the CMB cluster lensing signal; in §2 we develop a maximum likelihood approach to constraining this signal; §3 describes the generation and analysis of mock data, the results of which are presented in §4. Conclusions are given in §5. Throughout, we assume a flat-ΛCDM cosmology with $h = 0.7$ and $\Omega_M = 0.276$.

CHAPTER 1

BACKGROUND

1.1 The Unlensed CMB

The primordial CMB is thermal radiation originating from the end of the epoch of recombination, during which protons and electrons came together to form neutral atoms. Before recombination, the photon and electron plasmas were tightly coupled due to Thompson scattering. As the Universe cooled and became neutral, the mean free path of CMB photons increased dramatically. Although the Universe has since become ionized, the majority of CMB photons that we observe today have traveled without significant electromagnetic interaction since they last scattered at the end of recombination. It is the gravitational interactions experienced by CMB photons since the time of last scattering that concerns us here.

The CMB has a uniform temperature to one part in 10^5 owing to the homogeneity of the primordial plasma. Small fluctuations in the temperature of the CMB are the result of acoustic oscillations in this plasma. The theory of Inflation [Guth, 1981, Linde, 1982] posits that the perturbations that initially sourced these oscillations (long before recombination) are drawn from a very-nearly Gaussian distribution. As these perturbations grow essentially linearly until well after the time of last scattering, the anisotropies in the CMB are also predicted to be very close to Gaussian. And indeed, observations to date have found no evidence for departures from Gaussianity [Planck Collaboration et al., 2013]. To a very high level of accuracy the primordial unlensed CMB can be treated as a Gaussian random field.

All of the information about a Gaussian random field is captured in its power spectrum. As a result of photon diffusion (Silk Damping) at the time of recombination, power on scales below about 14' – corresponding to multipole $l \sim 800$ – is highly suppressed in the primordial CMB. Several generations of CMB experiments have jointly measured the power spectrum of the CMB with impressive accuracy out to $l \lesssim 10000$ [e.g. Hinshaw et al., 2013, Planck

collaboration et al., 2013, Keisler et al., 2011, George et al. in prep., 2014]. Therefore, over the multipole range at which it has significant power, the statistical properties of the primordial CMB are known with exquisite precision. This fact is essential to our ability to detect slight distortions in this random field due to gravitational lensing. The CMB power spectrum is shown in Fig. 1.2.

1.2 Gravitational Lensing of the CMB

Gravitational lensing results in a remapping of CMB photons to new (lensed) positions on the sky. Since the shape of the null geodesics along which photons travel is independent of frequency, so too is the remapping caused by gravitational lensing. Furthermore, for our purposes, gravitational lensing does not change photon energies. A photon falling into a gravitational potential well will gain energy, but if the potential does not evolve significantly during the photon's traversal, the photon will lose an equivalent amount of energy on its way out of the well; the net result is no energy change. We are primarily interested in lensing by galaxy clusters which are sufficiently compact that their potential wells do not evolve significantly during photon crossing and so the photon energy remains constant[1]. As a consequence of Liouville's theorem and the fact that gravitational lensing does not change photon energies, the remapping caused by gravitational lensing preserves surface brightness. As a result, for a perfectly uniform CMB the effects of lensing are entirely unobservable. It is the presence of small anisotropies in the CMB that make measurement of the lensing effect possible. Gravitational lensing of the CMB has been covered in great detail in the literature [for an excellent review see Lewis and Challinor, 2006]. Here we concentrate on the formalism necessary to model CMB cluster lensing.

Lensing alters the directions of photons so that a photon that is observed at direction $\hat{n}$ would have been observed at direction $\hat{n} - \vec{\delta}(\hat{n})$ in the absence of lensing, where $\vec{\delta}(\hat{n})$ is the

1. When the potential well is very large, significant evolution can occur during photon crossing and a significant distortion to the CMB can result, i.e. the integrated Sachs-Wolfe Effect [Sachs and Wolfe, 1967]

deflection field. With this sign convention, the deflection field takes unlensed positions to lensed positions. For the most part, we will work in the flat sky approximation under which the temperature field, $T(\vec{\theta})$, can be considered a function of the two-dimensional vector $\vec{\theta}$. As we will be interested in gravitational lensing of the CMB in small patches on the sky near galaxy clusters, this approximation is well motivated. The lensed temperature field, $T^{len}(\vec{\theta})$, can then be related to the unlensed temperature field, $T^{unlen}(\vec{\theta})$, via

$$\begin{aligned} T^{len}(\vec{\theta}) &= T^{unlen}(\vec{\theta} - \vec{\delta}(\vec{\theta})) \\ &\approx T^{unlen}(\vec{\theta}) - \vec{\delta}(\vec{\theta}) \cdot \nabla T^{unlen}(\vec{\theta}), \end{aligned} \tag{1.1}$$

where in the second line we have Taylor expanded the temperature field to first order in the angular coordinate.

Fourier transforming Eq. 1.1 results in

$$T^{len}(\vec{l}) \approx T^{unlen}(\vec{l}) - \frac{i}{2\pi} \int d^2l \, \vec{l}' \cdot \vec{\delta}(\vec{l} - \vec{l}') T^{unlen}(\vec{l}'), \tag{1.2}$$

where $\vec{l}$ is the Fourier conjugate to $\vec{\theta}$. Eq. 1.2 shows that the observed temperature at one multipole is related to the temperature at all other multipoles through the deflection field, $\vec{\delta}$. Thus we see that lensing induces correlations between different l modes on the sky and the lensed temperature field is therefore no longer Gaussian (for a Gaussian random field different l-modes are uncorrelated). Note, however, that the lensed temperature field is just a remapping of a Gaussian field; if the deflection field is known, the lensed CMB can still be described by a Gaussian likelihood as long as positions in the map are adjusted to account for the deflections.

Eq. 1.1 shows that the lensed temperature field correlates the unlensed temperature field with its gradient. This fact has been exploited to develop estimators for the deflection field, many of which are based on the optimal quadratic estimator of Hu [2001] and Hu and Okamoto [2002]. Quadratic estimators effectively estimate the lensing potential $\phi(\vec{\theta})$

(defined such that $\vec{\delta}(\vec{\theta}) = \nabla\phi(\vec{\theta})$) by forming the product of a measured CMB map with its gradient, filtered and weighted in such a way as to make an unbiased estimate of ϕ with minimal variance. It should be emphasized that while the estimator of Hu [2001] and Hu and Okamoto [2002] is the minimum variance *quadratic estimator* for the lensing potential, it is not necessarily the true minimum variance estimator.

In principle, CMB lensing quadratic estimators could be applied to the CMB in the vicinity of clusters to extract constraints on the cluster lensing potential.[2] These lensing potential constraints could then be used to place constraints on the masses of clusters by e.g. fitting to a model mass distribution. As we discuss in more detail below, we have chosen a different approach to constraining the CMB lensing signal that relies on identifying the true maximum likelihood estimator for the cluster mass given a model for its mass distribution.

1.3 Galaxy Clusters

Galaxy clusters are the largest bound structures in our Universe, having masses roughly in the range $10^{14}\,\mathrm{M}_\odot$ to $2\times10^{15}\,\mathrm{M}_\odot$. The majority of the cluster mass (typically about 90%) is in the form of a halo of weakly interacting dark matter that extends considerably beyond the visible galaxies in the cluster. Because clusters are so massive, intracluster gas (which makes up about 10% of the cluster mass) is virially heated to temperatures on the order of

$$kT \sim \frac{GMm_p}{2R} = 7\,\mathrm{keV}\left(\frac{\mathrm{M}}{3\times10^{14}\,\mathrm{M}_\odot}\right)\left(\frac{1\,\mathrm{Mpc}}{\mathrm{R}}\right) \tag{1.3}$$

where M is the mass of the cluster, R is its effective radius and m_p is the mass of a proton. This hot, ionized gas is responsible for the Sunyaev-Zel'dovich effect, which will be discussed in more detail in §1.5. Note that Eq. 1.3 is slightly misleading as it hides the dependence of

2. As discussed in Hu et al. [2007a], applying the standard quadratic estimator of Hu [2001] and Hu and Okamoto [2002] to the CMB near clusters can result in a bias caused by assuming that the deflection is a small perturbation to the source field. This bias can be removed, however, with an appropriate filtering scheme [Hu et al., 2007a].

R on M.

Dark matter-only N-body simulations suggest that cluster mass profiles are reasonably well fit by the Navarro-Frenk-White (NFW) profile, first proposed in Navarro et al. [1996]. The NFW profile is given by

$$\rho(r) = \frac{\delta_c \rho_{crit}(z)}{(rc/r_{200})(1 + rc/r_{200})^2}, \tag{1.4}$$

where $\rho(r)$ is the mass density at distance r from the center of the cluster and $\rho_{crit}(z) = 3H^2(z)/(8\pi G)$ is the critical density for closure of the Universe at redshift z. r_{200} is the virial radius of the cluster, defined such that average mass density enclosed with r_{200} is equal to $200\rho_{crit}(z)$. The total mass enclosed within r_{200} is then

$$M_{200} = \frac{800\pi}{3}\rho_{crit}(z) r_{200}^3. \tag{1.5}$$

For the analysis presented here we consider M_{200} to be the parameter of interest rather than r_{200}. The concentration parameter, c, controls how centrally concentrated the density profile is. Fits to simulations suggest that c is a slowly varying function of the cluster mass and redshift; for a $M = 5 \times 10^{14}\,\mathrm{M}_\odot$ cluster, the expected concentration is $c \sim 2.7$ [Duffy et al., 2008]. δ_c is fixed to

$$\delta_c = \frac{200}{3}\frac{c^3}{\ln(1+c) - c/(1+c)} \tag{1.6}$$

by the requirement that M_{200} and r_{200} are related as in Eq. 1.5.

While the NFW profile is a common choice for parameterizing the mass distributions of clusters, it is well known that such profiles provide only an approximate description of real clusters [e.g. Merritt et al., 2006, Duffy et al., 2010]. High resolution simulations, for instance, suggest that the density profiles of the inner cores of clusters are flatter than predicted by the NFW profile (which diverges as r^{-1} for small r) [e.g. Merritt et al., 2006, Navarro et al.,

2010]. Furthermore, while baryons make up only a small fraction of the total cluster mass, their ability to cool efficiently allows them to condense towards the cluster center, which in turn can increase the dark matter density in these regions [e.g. Gnedin et al., 2004, 2011]; other baryonic effects such as supernovae and AGN feedback may further impact the density profile [Duffy et al., 2010]. Finally, simulations also suggest that halos of galaxy clusters are triaxial, rather than spherically symmetric as assumed in the NFW profile [Jing and Suto, 2002]. Still, despite these qualifications, the NFW profile has proven an excellent fit to the observed density profiles of clusters obtained via weak lensing measurements [Newman et al., 2013]. The NFW profile is more than adequate for our purposes since we are interested here in only a first detection of the CMB cluster lensing signal and do not expect to be sensitive to the details of the halo shape. Future work may attempt to improve upon the accuracy of the halo modeling presented here.

1.4 The Lensing Signal from Galaxy Clusters

As argued by Seljak and Zaldarriaga [2000], regardless of the detailed form of $\vec{\delta}(\vec{\theta})$, cluster lensing leads to a characteristic imprint in the CMB near galaxy clusters. Since the primordial CMB has little power below scales of ~ 10 arcminutes due to diffusion damping and the deflections are ~ 1 arcminute (as we will see below), the CMB can be considered a pure gradient in the vicinity of the cluster. Eq. 1.1 then suggests several important features of the CMB cluster lensing signal. First, the size of the signal is proportional to the gradient of the CMB; if the gradient vanishes, so does the lensing signal. Second, consider the fact that photons passing near the cluster will be deflected towards the cluster so that they *appear* farther away from the cluster; $\vec{\delta}(\vec{\theta})$ will therefore in general point away from the cluster. Consequently, from Eq. 1.1 we see that the lensed temperature field will be decreased on the positive side of the gradient and will be increased on the negative side. The result is the characteristic dimple pattern shown in Fig. 1.1. For this figure we have assumed a $M = 10^{15}\,\mathrm{M}_\odot$ cluster at $z = 1$ that is described by an NFW profile with $c = 3$. We place

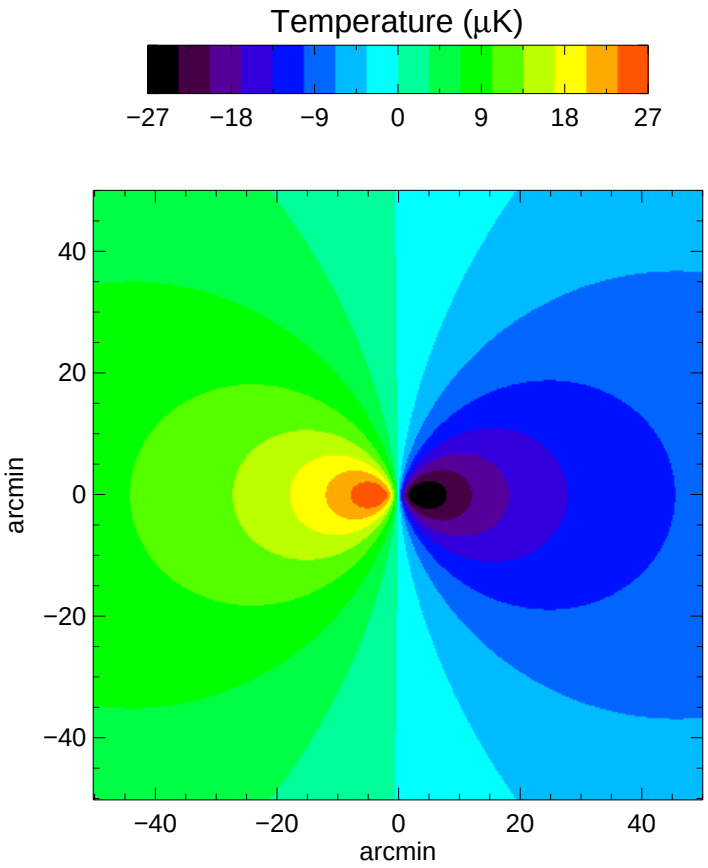

Figure 1.1: Difference between lensed and unlensed CMB for a $M = 10^{15}\,\mathrm{M}_\odot$ cluster at $z = 1$ sitting on top of a pure gradient in the CMB with amplitude $13\,\mu$K/arcmin. We assume an NFW mass profile for the cluster with $c = 3$.

this cluster on top of a pure gradient with amplitude $13\,\mu$K/arcmin. Since the CMB has an RMS of $\sim 115\,\mu$K and a coherence length of about 10 arcminutes, this value of the gradient is fairly typical.

For even the most massive galaxy clusters, gravitationaly lensing causes the CMB to be deflected by at most an arcminute. It is appropriate, then, to assume the Born approximation under which the gravitational potential experienced by a photon is evaluated along the undeflected photon path. Furthermore, as the distance over which a photon feels the effects of gravitational lensing by a cluster is small compared to the total distance traveled, it is also appropriate to make a thin lens approximation, under which the three-dimensional mass

distribution of the cluster can be replaced by a projected two-dimensional mass distribution. Finally, for simplicity, we consider a rotationally symmetric mass distribution. Making these approximations, the deflection angle due to the cluster is

$$\vec{D}(\vec{\theta}) = -8\pi G \frac{\vec{\theta}}{|\vec{\theta}|} \frac{(\chi_S - \chi_L)}{\chi_S} \left[\frac{1+z_L}{\theta \chi_L} \int_0^{\chi_L \theta/(1+z_L)} dR\, R\Sigma(R) \right], \tag{1.7}$$

where $\chi_S = 1.4 \times 10^4$ Mpc and χ_L are the comoving distances to the last scattering surface (source) and the cluster (lens), respectively, and $\Sigma(R)$ is the 2D projected mass distribution of the cluster [Dodelson and Starkman, 2003]. Note that there is a subtle distinction between the $\vec{D}(\vec{\theta})$ of Eq. 1.7 and the $\vec{\delta}(\theta)$ considered previously. Consider a photon that originates at position $\vec{\theta}_0$ but – because of lensing – appears at position $\vec{\theta}$. From our previous definition, we have $\delta(\vec{\theta}) = \vec{\theta} - \vec{\theta}_0$. On the other hand, with the definition in Eq. 1.7 we have $\vec{D}(\theta_0) = \vec{\theta} - \vec{\theta}_0$. In other words, $\vec{D}$ should be evaluated at unlensed positions, while $\vec{\delta}$ should be evaluated at lensed positions.

As described above, a reasonable cluster mass distribution to assume is the NFW profile of Eq. 1.4. For an NFW mass distribution located at angular diameter distance $d_L = \chi_L/(1+z_L)$ from the observer, photons originating from a source at angular diameter distance $d_S = \chi_S/(1+z_S)$ and angle $\vec{\theta}$ with respect to the source will be deflected by an angle

$$\vec{D}\,(\theta) = \frac{16\pi G A}{c r_{200}} \frac{\vec{\theta}}{\theta} \frac{d_{SL}}{d_S} g(d_L \theta c / r_{200}), \tag{1.8}$$

where $d_{SL} = (\chi_S - \chi_L)/(1+z_S)$ is the angular diameter distance between the source and the lens [Dodelson, 2004a]. The function $g(x)$ is given by

$$g(x) = \frac{1}{x} \begin{cases} \ln(x/2) + \frac{\ln\left(x/[1-\sqrt{1-x^2}]\right)}{\sqrt{1-x^2}}, & \text{if } x < 1 \\ \ln(x/2) + \frac{\pi/2 - \arcsin(1/x)}{\sqrt{x^2-1}}, & \text{if } x > 1 \end{cases} \tag{1.9}$$

and the constant A is related to M_{200} and c via

$$A = \frac{M_{200}c^2}{4\left[\ln(1+c) - c/(1+c)\right]}. \tag{1.10}$$

We have chosen here to parameterize the deflection angle model in terms of M_{200} and c (r_{200} in Eq. 1.8 is related to M_{200} via Eq. 1.5). For a $c = 3$ cluster with mass $M_{200} = 5 \times 10^{14}\,\mathrm{M}_\odot$ located at $z = 1$, the peak deflection is ~ 0.5 arcmin at about 2 arcmin away from the cluster. Note that in our analysis we allow the cluster mass to be negative; a negative cluster mass simply means that the deflection vector is pointed in the opposite direction as it would be for a positive cluster mass.

1.5 The Sunyaev-Zel'dovich Effect

Gravitational lensing is not the only source of distortion to the primordial CMB. The Sunyaev-Zel'dovich effect (SZE) is the distortion of the CMB induced by inverse-Compton scattering of CMB photons and energetic electrons [for a review see Birkinshaw, 1999]. This effect is especially pronounced in the directions of massive galaxy clusters as these objects are reservoirs of hot, ionized gas. The magnitude of the CMB distortion induced by the SZE effect can be significantly greater than that induced by CMB cluster lensing. SZ surveys such as the South Pole Telescope SZ Survey, for instance, routinely detect individual clusters [e.g. Staniszewski et al., 2009] via the SZE (this is, after all, one of the primary goals of such surveys); the CMB cluster lensing signal, on the other hand, has not been detected and is unlikely to be detected for single clusters in the near future. Because of the large magnitude of the SZE and the fact that the SZE and CMB cluster lensing signals overlap spatially (they are both most pronounced within several arcminutes of galaxy clusters), the SZE is a potentially serious contaminant for measurement of CMB cluster lensing and warrants careful consideration.

The SZE from clusters can be divided into two parts: the thermal SZE and the kinematic

SZE. The thermal SZE results from inverse-Compton scattering of CMB photons with hot cluster gas. An interesting feature of the thermal SZE (and one that makes the SZE particularly interesting as a cosmological probe) it that the amplitude of the signal is independent of cluster redshift. Unlike gravitational lensing, the inverse-Compton scattering process that gives rise to the SZE results in a spectral distortion of the CMB. Because the cluster electrons have temperatures far in excess of the CMB, the scattering process typically causes CMB photons to gain energy, leading to a decrease in the CMB intensity in the Raleigh-Jeans regime and an increase in the Wien regime. More explicitly, the spectral shape of the distortion is given by

$$f(x) = \left(x\frac{e^x + 1}{e^x - 1} - 4 \right) (1 + \delta_{SZ}(x, T_e)), \tag{1.11}$$

where $x = h\nu/k_B T_{CMB}$ is a dimensionless version of the frequency of observation, ν, T_e is the electron temperature in the cluster and δ_{SZ} is a relativistic correction [Plagge et al., 2010]. In the non-relativistic limit, the spectral shape of the distortion is independent of T_e, having a minima at roughly 130 GHz, a maxima at 370 GHz and no distortion at approximately 220 GHz. The frequency-dependence of the effect will be essential to our attempts to eliminate SZE contamination of our cluster lensing analysis.

The temperature change in the CMB due to the SZE is related to the Compton y-parameter, which is a measure of the integrated pressure along the line of sight:

$$\frac{\Delta T}{T_{CMB}} = f(x)y = \frac{f(x)\sigma_T}{m_e} \int P(l)dl, \tag{1.12}$$

where $P(l) = n_e T_e$ is the cluster pressure at line of sight position l, equal to the product of the electron number density, n_e, and temperature. Building on the work of Nagai et al. [2007], Arnaud et al. [2010] fit a well-motivated pressure profile to a combination of observational data and simulations. Their best fit model, expressed as a function of distance from the

cluster center, r, is:

$$P(r) = 1.65\,\mathrm{eV\,cm^{-3}} E^{8/3}(z) \left(\frac{M_{500}}{3\times10^{14}\,\mathrm{M_\odot}}\right)^{0.79} p(r/r_{500}), \tag{1.13}$$

where M_{500} is the mass enclosed in a sphere of radius r_{500}, defined such that the mean mass within the sphere is equal to 500 times the critical density (i.e. exactly analogous to r_{200}). $p(x)$ is a dimensionless pressure profile that is assumed to follow the generalized NFW form introduced in Nagai et al. [2007]:

$$p(x) = \frac{8.403}{(c_{500}x)^\gamma\left[1+(c_{500}x)^\alpha\right]^\delta}, \tag{1.14}$$

where $c_{500} = 1.177$, $\alpha = 1.051$, $\gamma = 0.3081$ and $\delta = 4.931$ [Arnaud et al., 2010]. With this profile, an NFW cluster with $M_{200} = 5\times10^{14}\,\mathrm{M_\odot}$ and $c = 3$ causes a decrement in the CMB with magnitude $\Delta T = -400\,\mu\mathrm{K}$ when observed at 150GHz. This means that the SZE is about an order of magnitude larger than the cluster lensing signal we are attempting to detect.

The kinematic SZE results from the inverse-Compton scattering of CMB photons with electrons that have bulk velocities relative to the Hubble flow. Here we consider the kinematic SZE due to electrons residing in a galaxy cluster. Bulk motions of cluster electrons could be due, for instance, to the cluster falling towards nearby superstructures or because the cluster is rotating. In the rest-frame of the moving electrons, Doppler shifting causes the CMB to appear non-isotropic; scattering then slightly re-isotropizes this radiation. To a distant observer, the effect results in a distortion to the CMB spectrum. The magnitude of the effect, $\Delta T/T$, is proportional to $\tau_e v_z/c$, where τ_e is the optical depth of the electrons and v_Z is the velocity of the bulk flow along the line of sight direction [Sunyaev and Zeldovich, 1972]. For high mass clusters with $M \gtrsim 10^{15}\,\mathrm{M_\odot}$, the thermal SZE is expected to dominate over the kinematic SZE by a factor of ~ 20; for clusters with $M \sim 10^{13}\,\mathrm{M_\odot}$ the two effects should have comparable magnitudes [Hand et al., 2012]. The kSZ has only recently been

detected via cross-correlation with data from the Atacama Cosmology Telescope and the Baryon Oscillation Spectroscopic Survey [Hand et al., 2012]. Unlike the thermal SZE, the kinematic SZE preserves the blackbody form of the CMB spectrum while only changing its temperature [Sunyaev and Zeldovich, 1972]; in the non-relativistic limit, the maximum intensity of the kinematic SZE corresponds to the null of the thermal SZE [Birkinshaw, 1999].

1.6 Foregrounds

CMB telescopes observe a combination of radiation from the CMB and foreground sources. Foreground emission must be taken into account when searching for the cluster lensing signal. Some sources – like active galactic nuclei and bright dusty star forming galaxies (DSFGs) – are bright enough that they can be detected as point sources in the data and masked [Mocanu et al., 2013]. Faint sources that are too dim to be detected individually contribute to the Cosmic Infrared Background (CIB) which must be considered as an additional source of noise to the measurement of CMB cluster lensing. The dominant contribution to the CIB comes from UV and optical photons that are absorbed by dust and re-emitted in the infrared (i.e. DSFGs). The contributions from these unresolved sources can be divided into two components: a Poisson part and a clustered part [Keisler et al., 2011]. Another source of foreground power considered in Keisler et al. [2011] is the SZE from large scale structure and unresolved sources. As we discuss in §2.3, the SZE foreground contribution is removed using frequency information so it not necessary to consider the unresolved SZE as an additional foreground.

The Poisson foreground is due to Poisson fluctuations in the number of unresolved sources across the sky. For the faint sources that we are concerned with here, there are many sources per square arcminute (roughly the scales of interest to our measurement of CMB cluster lensing) so it is reasonable to model the Poisson contribution as Gaussian with $C_l = C^{\rm Poisson}$, where $C^{\rm Poisson}$ is independent of l. No physical contribution to the sky can have power to

arbitrarily large l; the Poisson power must be cut off at some $l_{max}^{\rm Poisson}$ that corresponds to the sizes of the sources contributing to this background. Since these sources are predominantly DSFGs the cutoff scale corresponds to the angular size of a galaxy, which is roughly 1 arcsecond or $l \sim 6.5 \times 10^5$. As will be discussed in more detail later, the telescope beam function cuts off power at scales significantly below $l_{max}^{\rm Poisson}$ so the precise value of $l_{max}^{\rm Poisson}$ is unimportant. At high l, $C^{\rm Poisson}$ dominates the total measured power spectrum so the value of $C^{\rm Poisson}$ can be determined directly from the data, as we discuss in §2.4. The Poisson power spectrum is shown in Fig. 1.2.

Clustering of the emissive point sources (DSFGs) introduces additional correlated foreground noise to the data that is not captured by $C_l = C^{\rm Poisson}$. Following Shirokoff et al. [2011], Millea et al. [2012] and Keisler et al. [2011] we assume that the contribution from clustered point sources is described by $D_l \equiv l(l+1)C_l/(2\pi) = \frac{D_{3000}}{f(3000)} f(l)$, where $f(l) = 1$ for $l < 1500$ and $f(l) = \left(\frac{l}{1500}\right)^{0.8}$ for $l \geq 1500$. D_{3000} sets the normalization of this component at $l = 3000$ and has units of $\mu{\rm K}^2$. This template for the clustered power spectrum captures contributions from both linear and non-linear regimes. Fig. 1.2 shows the power spectrum of the clustered component.

The foreground models described above were derived from studying the observed CIB emission away from clusters. Consequently, while these models may incorporate the effects of gravitational lensing by large scale structure, they do not include any effects of lensing by the cluster. Whether or not the foregrounds are lensed by a cluster depends on the redshift from which the foreground emission emanates relative to the redshift of the cluster; foreground emission from in front of the cluster, for instance, will not be lensed. Unfortunately, because it is difficult to resolve the CIB into individual sources, the redshift distribution of these sources has proved difficult to constrain. Not surprisingly, the redshift distribution of sources contributing to the CIB also varies with frequency. An analysis of data from the *Herschel* Multi-tiered Extragalactic Survey by Béthermin et al. [2012] suggests that the redshift distribution of sources contributing to the CIB is quite broad, with support across

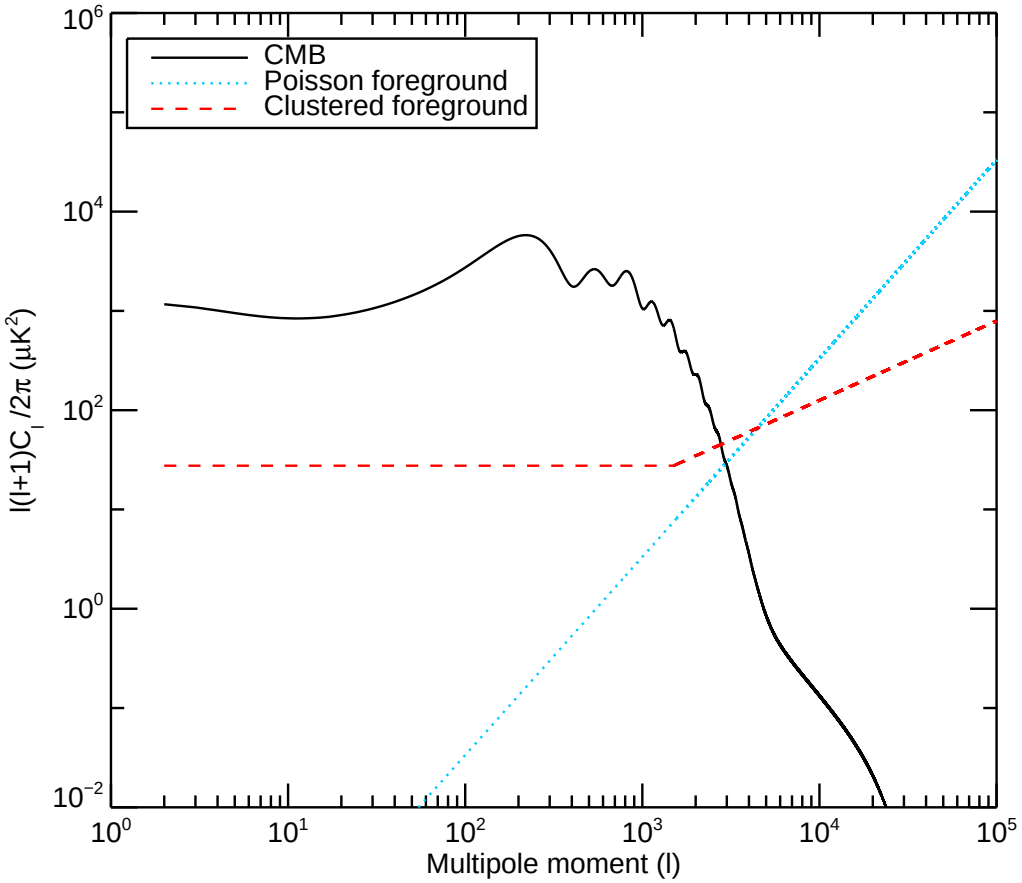

Figure 1.2: The power spectra of the components in our model.

$z = 0$ to $z \gtrsim 3$, although the observation frequencies in Béthermin et al. [2012] were higher than those of interest here. A recent (and preliminary) analysis of Planck data by Schmidt et al. [2014] suggests that for frequencies between about 200 GHz and 550 GHz, the redshift distribution of the CIB is again broad (covering a redshift range from $z = 0$ to $z = 4$) with a peak near $z \sim 1.5$. Since the majority of clusters we are interested in have redshifts in the range $z = 0.5$ to $z = 1.5$, it is reasonable to assume that some fraction of the Poisson and clustered foreground emission will be lensed and some will remain unlensed.

CHAPTER 2

ANALYSIS

We adopt a maximum likelihood approach to measuring the CMB cluster lensing signal. Below, we derive the full pixel-space likelihood for the lensed CMB given a model for the lensing deflections. By evaluating the likelihood for the observed data as a function of our model parameter, M_{200}, we obtain CMB-lensing constraints on the cluster mass. Because this approach uses the exact likelihood for the data given our model, it necessarily contains all the available information about gravitational lensing in the data and therefore is the optimal way of extracting the signal.

2.1 The Unlensed CMB

We first review the calculation of the likelihood function for the primordial, unlensed CMB. In this context, the likelihood refers to the probability of measuring some set of pixelized temperature values on the sky, $\vec{d}$, given an underlying model for the data. The Gaussian nature of the primordial CMB means that the likelihood can be written as

$$\mathcal{L}(\vec{d}; C) = \frac{1}{(2\pi)^{N_{pix}/2}\sqrt{\det(C)}} \exp\left[-\frac{1}{2}\vec{d}^T C^{-1}\vec{d}\right], \tag{2.1}$$

where $\vec{d}$ is an N_{pix} element data vector and C is the $N_{pix} \times N_{pix}$ covariance matrix that is predicted by a model. The covariance matrix can in general be split into two parts, $C = C_S + C_N$, where C_S is the covariance of the underlying sky signal and C_N is the instrumental noise covariance added by the telescope. The data are assumed to be mean-subtracted so that $\langle\vec{d}\rangle = 0$.

We now turn to calculating C_S, following somewhat closely the derivation presented in

Dodelson [2003]. The signal covariance matrix elements $C_{S,ij}$ are defined such that

$$C_{S,ij} = \langle s_i s_j \rangle - \langle s_i \rangle \langle s_j \rangle \quad (2.2)$$

$$= \langle s_i s_j \rangle, \quad (2.3)$$

where the expectation value should be taken over different realizations of the sky signal. Again, we are assuming that the mean signal has been subtracted so that $\langle s_i \rangle = 0$. The signal in a single pixel, s_i, depends on the true temperature field across the sky, $\Theta(\hat{n})$, how the true sky signal gets processed into a map by the telescope and data reduction, and the pixelization that is applied by the analyst. Prior to the pixelization, the processing of the sky signal can be divided into a part due to the telescope beam (the 'beam function'), and a part due to filtering applied to the data timestream (the 'transfer function'). For the most part, the beam and transfer functions can be lumped together into a single transformation that acts on the data. For ease of notation we will follow this approach below.

The application of the telescope beam (really the beam and transfer function) to the sky turns the field $\Theta(\hat{n})$ into a new field, $\Theta_{beam}(\hat{n})$, given by

$$\Theta_{beam}(\hat{n}) = \int d\hat{n}' \, \Theta(\hat{n}') B(\hat{n}', \hat{n})$$

$$= \int d\hat{n}' \, \Theta(\hat{n}') B(\hat{n}' - \hat{n}), \quad (2.4)$$

where $B(\hat{n}', \hat{n})$ encapsulates the effects of the beam and transfer function. The second equality follows from assuming that the beam is constant across the sky [1].

Pixelization causes the signal in a single pixel, s_i, to be equal to an integral across Θ_{beam}

1. While the telescope beam remains fairly constant across the sky, the transfer function varies considerably across different patches. We consider each patch separately so this assumption remains valid.

weighted by the pixel window function $P_i(\hat{m})$:

$$\begin{aligned} s_i &= \int d\hat{m}\, \theta_{beam}(\hat{m}) P_i(\hat{m}) \\ &= \int d\hat{m}\, \theta_{beam}(\hat{m}) P(\hat{m} - \hat{m}_i) \\ &= \int d\hat{n}'\, \Theta(\hat{n}') \int d\hat{m}\, P(\hat{m} - \hat{m}_i) B(\hat{n'} - \hat{m}) \\ &\equiv \int d\hat{n}'\, \Theta(\hat{n}') R(\hat{n}, \hat{m}_i), \end{aligned} \tag{2.5}$$

where in the last line we have defined the combined pixel-beam function:

$$R_i(\hat{n}) = \int d\hat{m}\, P(\hat{m} - \hat{m}_i) B(\hat{n} - \hat{m}), \tag{2.6}$$

and we have assumed that the pixel window function does not vary across the sky. The area-preserving projection scheme that we use for generating two-dimensional maps from curved sky observations ensures that this approximation is a good one.

Having expressed the observed signal in terms of the true $\Theta(\hat{n})$, we now decompose $\Theta(\hat{n})$ into a spherical harmonic basis:

$$\Theta(\hat{n}) = \sum_{l=1}^{\infty} \sum_{m=-l}^{l} a_{lm} Y_{lm}(\hat{n}). \tag{2.7}$$

With this decomposition, the signal covariance matrix can be written as

$$\begin{aligned} C_{S,ij} &= \langle s_i s_j \rangle \\ &= \int d\hat{n} \int d\hat{n}'\, R_i(\hat{n}) R_j(\hat{n}') \sum_{l,m} Y_{lm}(\hat{n}) \sum_{l',m'} Y^*_{l'm'}(\hat{n}') \langle a_{lm} a^*_{l'm'} \rangle. \end{aligned} \tag{2.8}$$

The unlensed CMB has no preferred direction, which means that $\langle a_{lm} a^*_{l'm'} \rangle$ satisfies

$$\langle a_{lm} a^*_{l'm'} \rangle = \delta_{ll'} \delta_{mm'} C_l. \tag{2.9}$$

The sums in Eq. 2.8 then collapse to give

$$\begin{aligned} C_{S,ij} &= \int d\hat{n} \int d\hat{n}' \, R_i(\hat{n}) R_j(\hat{n}') \sum_l C_l \sum_m Y_{lm}(\hat{n}) Y^*_{lm}(\hat{n}') \\ &= \int d\hat{n} \int d\hat{n}' \, R_i(\hat{n}) R_j(\hat{n}') \sum_l C_l \frac{(2l+1) P_l \left[\hat{n} \cdot \hat{n}'\right]}{4\pi} \\ &\equiv \sum_l \frac{2l+1}{4\pi} C_l W_{l,ij} \end{aligned} \tag{2.10}$$

where

$$W_{l,ij} \equiv \int d\hat{n} \int d\hat{n}' \, R_i(\hat{n}) R_j(\hat{n}') P_l \left[\hat{n} \cdot \hat{n}'\right], \tag{2.11}$$

and P_l is the lth Legendre polynomial.

It is convenient at this point to introduce the flat-sky limit in which a small patch of the sky is approximated as a two dimensional plane. This approximation is appropriate here because we are interested in the small region of CMB around a galaxy cluster, on the scale of tens of arcminutes. In this limit, $\hat{n} \cdot \hat{n}'$ can be replaced with $\cos(|\vec{x} - \vec{x}'|)$ where $\vec{x}$ and $\vec{x}'$ are two dimensional vectors specifying locations in the plane. Furthermore, in the limit of large l, $P_l(\cos x) \approx J_0(lx)$ where J_0 is the 0th order Bessel function of the first kin. The window function can then be re-written as

$$W_{l,ij} \approx \int d^2x \int d^2x' \, R_i(\vec{x}) R_j(\vec{x}') J_0\left(l|\vec{x} - \vec{x}'|\right). \tag{2.12}$$

Appoximating the Legendre polynomial as a Bessel function has a negligible impact on our analysis.

A more convenient form for the window function is found by expressing the Bessel function

in its integral representation:

$$\begin{aligned} W_{l,ij} &= \frac{1}{2pi}\int d^2x \int d^2x'\, R_i(\vec{x})R_j(\vec{x}') \int_0^{2\pi} d\phi\, e^{-il|\vec{x}-\vec{x}'|\cos\phi} \\ &= \frac{1}{2\pi}\int_0^{2\pi} d\phi \int d^2x \int d^2x'\, R_i(\vec{x})R_j(\vec{x}')e^{-i\vec{l}\cdot(\vec{x}-\vec{x}')}, \end{aligned} \tag{2.13}$$

where in the second line l has been promoted to a vector $\vec{l}$ such that the angle between $\vec{l}$ and $\vec{x}-\vec{x}'$ is ϕ. The window function then becomes

$$W_{l,ij} = \frac{1}{2\pi}\int_0^{2\pi} d\phi \left[\int d^2x\, R_i(\vec{x})e^{-i\vec{l}\cdot\vec{x}}\right]\left[\int d^2x'\, R_j^*(\vec{x}')e^{-il\cdot\vec{x}'}\right]^*. \tag{2.14}$$

The terms in square brackets are just the Fourier transform of $R_i(x)$:

$$\begin{aligned} \tilde{R}_i(\vec{l}) &= \int d^2x\, R_i(\vec{x})e^{-i\vec{l}\cdot\vec{x}} \\ &= \int d^2x\, R(\vec{x}-\vec{x}_i)e^{-i\vec{l}\cdot\vec{x}} \\ &= e^{-i\vec{l}\cdot\vec{x}_i}\int d^2x\, R(\vec{x})e^{-i\vec{l}\cdot\vec{x}} \\ &= e^{-i\vec{l}}\tilde{R}(\vec{l}). \end{aligned} \tag{2.15}$$

So finally, the window function can be written as

$$W_{l,ij} \approx \frac{1}{2\pi}\int_0^{2\pi} d\phi\, |\tilde{R}(\vec{l})|^2 e^{-i(\vec{x}_i-\vec{x}_j)}. \tag{2.16}$$

To speed up the evaluation of the unlensed covariance matrix, we build up a table of $C_{S,ij}$ as a function of $|\vec{x}_i-\vec{x}_j|$ and the angle between $\vec{x}_i-\vec{x}_j$ and the x-axis. The covariance matrix can then be evaluated quickly by interpolation. We compute the input CMB power spectrum, C_l, using CAMB[2]; this power spectrum is shown in Fig. 1.2. Note that our C_l model includes the effects of lensing by large scale structure..

2. http://camb.info

2.2 The Lensed Pixel-Pixel Covariance Matrix

As discussed above, lensing changes the directions of photons so that a photon that is observed at $\hat{n}$ originally came from a direction $\hat{n}^{unlen} = \hat{n} - \vec{\delta}(\hat{n})$ where $\vec{\delta}(\hat{n})$ is the deflection field. This means that Eq. 2.7 must be replaced with

$$\begin{aligned} \Theta(\hat{n}) &= \sum_{l=1}^{\infty} \sum_{m=-l}^{l} a_{lm} Y_{lm}(\hat{n}^{unlen}) \\ &= \sum_{l=1}^{\infty} \sum_{m=-l}^{l} a_{lm} Y_{lm}(\hat{n} - \vec{\delta}(\hat{n})). \end{aligned} \tag{2.17}$$

Therefore the lensed covariance matrix element is

$$\begin{aligned} C_{S,ij} &= \int d\hat{n} \int d\hat{n}' \, R_i(\hat{n}) R_j(\hat{n}') \sum_l C_l \sum_m Y_{lm}(\hat{n} - \vec{\delta}(\hat{n})) Y^*_{lm}(\hat{n}' - \vec{\delta}(\hat{n}')) \\ &= \int d\hat{n} \int d\hat{n}' \, R_i(\hat{n}) R_j(\hat{n}') \sum_l C_l \frac{(2l+1)}{4\pi} P_l \left[(\hat{n} - \vec{\delta}(\hat{n})) \cdot (\hat{n}' - \vec{\delta}(\hat{n}')) \right]. \end{aligned} \tag{2.18}$$

Making a plane approximation we can write

$$\hat{n} - \vec{\delta}(\hat{n}) \approx \vec{x} - \vec{\delta}(\vec{x}) \tag{2.19}$$

where $\vec{x}$ and $\vec{\delta}(\vec{x})$ are vectors in the plane. Then we have

$$\begin{aligned} C_{S,ij} &\approx \int d^2x \int d^2x' \, R_i(\vec{x}) R_j(\vec{x}') \sum_l C_l \frac{(2l+1)}{4\pi} P_l \left(\cos \left| (\vec{x} - \vec{\delta}(\vec{x})) - (\vec{x}' - \vec{\delta}(\vec{x}')) \right| \right) \\ &\equiv \int d^2x \int d^2x' \, R_i(\vec{x}) R_j(\vec{x}') g(\vec{x} - \vec{\delta}(\vec{x}), \vec{x}' - \vec{\delta}(\vec{x}')), \end{aligned} \tag{2.20}$$

where we have defined

$$g(\vec{x}-\vec{\delta}(\vec{x}),\vec{x}'-\vec{\delta}(\vec{x}')) = \sum_l C_l \frac{(2l+1)}{4\pi} P_l\left(\cos\left|(\vec{x}-\vec{\delta}(\vec{x}))-(\vec{x}'-\vec{\delta}(\vec{x}'))\right|\right)$$
$$\approx \sum_l C_l \frac{(2l+1)}{4\pi} J_0\left(l\left|(\vec{x}-\vec{\delta}(\vec{x}))-(\vec{x}'-\vec{\delta}(\vec{x}'))\right|\right). \quad (2.21)$$

Eq. 2.20 reduces to Eq. 2.10 in the limit that there is no deflection.

It is difficult to simplify Eq. 2.20 further as we did in the unlensed case because the deflection vectors vary as a function of $\vec{x}$. It is possible, though, to directly integrate Eq. 2.20 numerically to calculate the covariance matrix elements. To perform this integration we rely on the VEGAS Monte Carlo integration algorithm, which uses importance sampling to improve the accuracy of standard Monte Carlo integration [Lepage, 1978].

Unfortunately, direct integration of Eq. 2.20 is not practical for the purposes of actually detecting CMB cluster lensing. As we will see, the covariance matrix must be computed many times for each cluster, and each evaluation requires some 10000 evaluations of Eq. 2.20 (since we use $N_{pix} \sim 100$). Rather than perform the full 4D integral in Eq. 2.20 to evaluate the lensed covariance matrix, we instead rely on simulations of the lensed sky. Generating these simulations requires generating many realizations of the unlensed covariance matrix (which is easy to compute using Eq. 2.16) at high resolution, lensing these realizations by deflecting pixels according to a deflection model, and applying the beam and transfer functions to these lensed maps. Each of these steps are described in more detail in §3. We then compute a lensed covariance matrix by computing the covariance matrix of the simulated data across many realizations. To confirm that this process works, we compare the covariance matrix computed from simulations to that computed by direct integration. This comparison is shown in Fig. 2.1. The results of our likelihood analysis (§4) suggest that the accuracy of the simulation method is sufficient for our needs.

For the deflection template we use the NFW deflection model given in Eq. 1.8. In our analysis we keep the concentration fixed to $c = 3$ (close to the expected concentration of

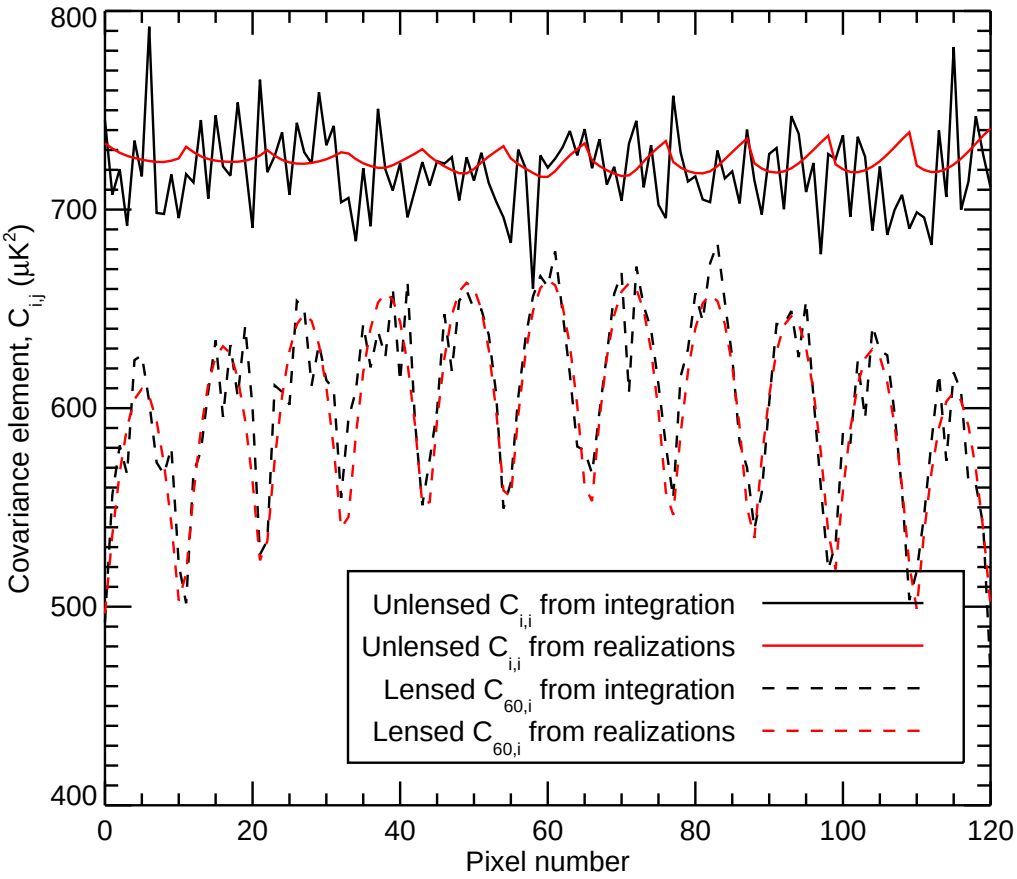

Figure 2.1: Comparison of two different methods for computing the lensed covariance matrix: direct integration and simulations (realizations). The jaggedness of the curve computed via direct integration is due to our use of a Monte Carlo method for evaluating the integral. The jaggedness of the curve computed via simulations is due to the finite number of samples. We prefer to compute the covariance matrix via simulations when possible as it is much less computationally expensive.

a $M = 5 \times 10^{14}\,\mathrm{M}_\odot$ cluster at $z = 1$) and evaluate the likelihood as a function of a single parameter, M_{200}. Our use of the NFW model with fixed concentration is motivated primarily by simplicity. Although the NFW profile may not be an exact match to the true cluster mass distribution, because we are interested only in obtaining a first detection of the CMB cluster lensing effect the NFW model should suffice for our purposes. In light of the problems with the NFW profile discussed above, the mass constraints that we obtain from our analysis should perhaps not be viewed as constraints on the true cluster mass, but rather constraints on an NFW fit to the cluster mass distribution. We save a more detailed treatment of the cluster mass distribution for future work.

2.3 Contamination from the Sunyaev-Zel'dovich Effect

As mentioned above, the thermal SZE results in a distortion to the CMB around galaxy clusters that has a magnitude significantly in excess of the distortion caused by gravitational lensing. As we demonstrate below (§4.2), simply ignoring the SZE results in a signficant bias. It is therefore important to consider methods for removing the SZE contamination.

The CMB distortion resulting from the SZE differs in two significant ways from the cluster lensing distortion. First, the morphology of the SZE on the sky differs from the lensing signal. The lensing signal generically looks like a dipole in the temperature field across the cluster. The thermal SZE, in contrast, looks like an overall increment or decrement in the temperature field across the cluster, depending on the frequency of observation. The magnitude of the thermal SZE (which dominates the total SZE signal) depends on the integral along the line of sight of the electron pressure in the cluster. In principle, given a model for the pressure distribution in the cluster – such as Eq. 1.13 – we can construct a model for the SZE that can then be incorporated into the likelihood in Eq. 2.1. By performing a joint fit for the parameters of both the SZE model and the lensing model we could extract constraints on lensing that are robust to contamination from the SZE. In practice, however, considerable variation in pressure profiles between different clusters makes this approach difficult. The

SZE signal can by quite complicated, owing for instance, to triaxiality of the halo and non-thermal pressure support. If the SZE model does not have sufficient freedom to fit these complicated morphologies, there will be significant residuals to the fit which may lead to bias in the lensing analysis. If, on the other hand, the SZE model does have sufficient freedom to fit the true SZE signal, some of the lensing signal may be fit out by the SZE model.

A second approach to dealing with thermal SZE contamination is to use spectral information. As discussed above, expressed in terms of brightness temperature fluctuations, the SZE is frequency dependent while the lensing signal is not. With multi-frequency observations, therefore, these two effects can be disentangled. The simplest approach – and the one we rely on here – is to create an 'SZE-free' map from a linear combination of multiband observations. As will be discussed in more detail below, the SPT observes at frequencies of 90, 150 and 200 GHz. The SZE-free linear combination of these three observation channels is created as follows. First, all three maps are smoothed to the resolution of the 90 GHz map since that map has the lowest angular resolution. Next, a linear combination of the 90 and 150 GHz maps that cancels the SZE while preserving the primordial CMB is generated; this is possible since the spectral weight of the SZE signal at both 90 and 150 GHz is known (Eq. 1.11). Lastly, this linear combination map is added to the 220 GHz map (which is assumed to be SZE-free already since 220 GHz corresponds to the null in the thermal SZE) with inverse variance weighting to minimize the noise in the final map. In the limit that the cluster electrons are non-relativistic, the map created in this way should be free of contamination from the thermal SZ. While this process removes (most) of the SZE contamination, it has two unfortunate consequences. For one, we have degraded the resolution of our maps to match the map with the worst resolution. Second, the final SZE-free map has about twice the noise level of the 150 GHz map (which is observed to greater depth than the 90 and 220 GHz maps).

2.4 Accounting for Foregrounds

As discussed in §1.6, Poisson and clustered foregrounds make a significant contribution to the measured data and should therefore be incorporated into our model covariance matrix. Some of the Poisson and clustered foreground emission likely comes from behind the galaxy clusters we are interested in, and is therefore lensed by these galaxy clusters. Accurately modeling the extent to which the foregrounds are lensed would require a model for the redshift distribution of the foregrounds. In the interest of simplicity, rather than attempt to generate such a model, we assume that the foregrounds are unlensed in our analysis. By analyzing mock data, we determine an upper limit to the bias introduced into our analysis by this assumption (see §4.3).

Templates for the power spectra of the Poisson and clustered foregrounds were presented in §1.6. The amplitude of the clustered foreground template is taken from Keisler et al. [2011], after adjusting to account for the fact that we use a linear combination of the three frequency maps (the SZE-free linear combination). The resultant normalization is $D_{3000} = 47\,\mu\mathrm{K}^2$. The amplitude of the Poisson template is determined on a field-by-field basis from SPT-data. The power spectrum is computed for each field in the range $5000 < l < 10000$ and the predicted clustering template is subtracted. The remaining power is dominated by the Poisson component and fitting a flat C_l model to the residual power yields its amplitude. Given the properly normalized templates for the C_l's of the Poisson and clustered foregrounds, we compute their contribution to the model covariance matrix using Eq. 2.16.

2.5 Additional Systematics

Above, we have considered two potentially important sources of systematic error: contamination from the SZE and uncertainty in the degree to which foregrounds are lensed. There are, however, several additional potential sources of systematic error that warrant some discussion: lensing by LSS, relativistic corrections to the SZE and the kinematic SZE.

In general, the amount of lensing experienced by the CMB is sensitive to a weighted integral of the matter distribution along the line of sight to the last scattering surface. This means that large scale structure in principle also contributes to lensing in the direction of clusters. On average, lensing by large scale structure should not bias the cluster lensing measurements as deflections towards the cluster are equally likely as deflections away from it. Since we consider stacking constraints from many clusters to achieve detection of the cluster lensing effect, lensing by LSS should not lead to a bias in our results. However, Metzler et al. [2001], Hoekstra [2003], Dodelson [2004b], Hoekstra et al. [2011] have argued that in the context of weak lensing shear measurements, LSS contributes a significant amount of noise to cluster mass constraints. Similar noise should be present in CMB cluster lensing constraints. However, since the noise level introduced by LSS is small relative to the strength of the expected stacked cluster lensing detection, we can safely ignore this effect [e.g. Seljak and Zaldarriaga, 2000].

As discussed in §1.5, relativistic effects induce a correction to the thermal SZE spectrum, $f(x)$, that depends on the electron temperature in the cluster, T_e. Since these effects are ignored when we create the SZE-free linear combination maps, residual thermal SZE contamination may result. However, the magnitude of the relativistic corrections is first order in kT_e/m_e [Itoh et al., 1998]. For typical cluster electron temperatures of 7 kev, the magnitude of these corrections is only $(7\,\mathrm{keV}/511\,\mathrm{keV}) \sim 0.01$ and can therefore be safely neglected in this work.

Finally, since the spectral shape of the kinematic SZE differs from that of the thermal SZE, the kinematic SZE will still be present in the SZE-free linear combination map described above. In fact, since the kinematic SZE preserves the blackbody form of the CMB (only changing its temperature), frequency information alone cannot be used to disentangle the kinematic SZE from primordial anisotropy. In principle, the morphology of the kinematic SZE could be used to separate it from the lensing signal. Any kinematic SZE due to bulk motion of the cluster relative to the Hubble flow should manifest itself as an overall increment

or decrement in the CMB temperature across the cluster. However, if the cluster is rotating, the kinematic SZE can appear as a dipole on the CMB, very similar to the expected signal from cluster lensing. Furthermore, as we show in §4.2 for the case of SZE contamination, just because a contaminant has a different morphology than the signal does not mean it cannot bias the lensing constraints.

Fortunately, as discussed above, the kinematic SZE is expected to be more than an order of magnitude below the thermal SZE and should therefore be smaller than the lensing signal (although perhaps not much smaller). Additionally, the kinematic SZE should be uncorrelated with the behvior of the CMB near the cluster, whereas the lensing signal will be highly aligned with the direction of the CMB gradient. We therefore expect that kinematic SZE contamination should not bias our lensing constraints, but rather introduce an extra source of noise. We save a detailed treatment of the effects of kinematic SZE contamination for future work.

2.6 Constraining CMB Cluster Lensing with the Likelihood

We now have all the ingredients necessary to constrain the masses of clusters using CMB cluster lensing. For a vector of measured temperature values, $\vec{d}$, around a single cluster we evaluate

$$\mathcal{L}(\vec{d}; M_{200}; z) = \frac{1}{(2\pi)^{N_{pix}/2}\sqrt{\det\left[C(M_{200}; z)\right]}} \exp\left[-\frac{1}{2}\vec{d}^{T}C^{-1}(M_{200}; z)\vec{d}\right]. \tag{2.22}$$

The model covariance, $C(M_{200}; z)$, can be broken into three parts:

$$C(M_{200}; z) = C^{primordial}(M_{200}; z) + C^{foregrounds} + C^{noise}, \tag{2.23}$$

where $C^{primordial}(M_{200}; z)$ is given by Eq. 2.20 and depends on the cluster mass and redshift through the deflection field template, $\vec{\delta}(M_{200})$, given in Eq. 1.8. $C^{primordial}(M_{200}; z)$ also

depends on the cosmological parameters through the C_l's. Since the cluster redshift is tightly constrained by other observations we do not allow it to vary in our analysis. $C^{foregrounds}$ is the unlensed foreground covariance matrix. As discussed above, our use of the unlensed foreground covariance matrix is not quite correct, but we will quantify the bias introduced into our analysis by this assumption. Finally, C^{noise} is measured from data as described in §3.1.

To constrain the cluster mass, we evaluate the likelihood across a grid of M_{200}. In principle, the covariance matrix needs to be evaluated for every cluster redshift and for each of the mass values that we explore. In practice, because the computation of the covariance matrix is computationally expensive, we find it preferable to first evaluate the covariance matrix across a relatively coarse grid of M_{200} and z. When evaluating the likelihood, we interpolate this table of covariance matrices to the desired mass and redshift.

Some confusion may arise from the fact that we use a Gaussian likelihood in Eq. 2.22 despite the fact that we have stated above that the lensed CMB is non-Gaussian. The lensed CMB is a remapped Gaussian random field. Given a *known* deflection field, our expression for the likelihood effectively undoes the effects of lensing so that correlations between points on the sky are evaluated in their *unlensed* positions. When written in this way, our use of a Gaussian likelihood to describe the lensed CMB is correct. However, this approach ignores the effects of lensing by LSS. The deflection angles caused by LSS are *unknown* and therefore cannot be 'undone' in our model covariance matrix. While we do incorporate the effects of lensing by LSS into our model C_l's, it is not strictly correct to use a Gaussian likelihood. We expect, though, that the error introduced into our analysis by this assumption is small.

Finally, because the CMB cluster lensing signal for a single cluster is well below the noise level of SPT, it is unlikely that we can obtain a detection of the effect from a single cluster. To obtain a detection, we must stack constraints from many (several hundred) clusters. We perform this stacking at the likelihood level, and consider a single M_{200} for all clusters. In

other words, we compute

$$\mathcal{L}^{\text{total}}(\{\vec{d}_i\}; M_{200}) = \prod_{i=1}^{N_{\text{clusters}}} \mathcal{L}(\vec{d}_i; M_{200}), \tag{2.24}$$

where N_{clusters} is the total number of clusters in our dataset. This method of stacking clusters is appealing because it is simple and because it depends only on the lensing signal. Unfortunately, when the likelihood is computed in this fashion, the final likelihood will necessarily be broadened by the inclusion of clusters with different masses.

Another approach to stacking the CMB cluster lensing constraints is to compute

$$\mathcal{L}^{\text{total}}_{\text{joint}}(\{\vec{d}_i, M_i\}; M_{200}/M_{\text{external}}) = \prod_{i=1}^{N_{\text{clusters}}} \mathcal{L}(\vec{d}_i; M_{200}/M_{\text{external},i}), \tag{2.25}$$

where $M_{\text{external},i}$ is the mass of the ith cluster as inferred by some other means (such as observed SZE decrement). Assuming that the lensing mass is related to the inferred mass by some scaling relation, i.e. $M_{200} = \alpha M_{\text{external},i}$, then the stacked likelihood considered as a function of $M_{200}/M_{\text{external},i}$ should be centered at α and will not be broadened by spread in the true cluster masses. In other words, this approach to stacking the likelihoods measures a scaling relation between the lensing mass and some other observable rather than the lensing mass alone.

CHAPTER 3

MOCK DATA

To test the techniques that we have developed for extracting the cluster lensing signal, we generate and analyze mock data. The mock data includes contributions from the lensed CMB, foregrounds, and instrumental noise. We have attempted to make the mock data as close as possible to data from the SPT-SZ Survey. To this end, we use realistic noise models, beam and transfer functions, and cluster selection (in mass and redshift).

3.1 The South Pole Telescope

The SPT is a 10-meter diameter telescope located at the South Pole (more details about the telescope can be found in Ruhl et al. [2004], Padin et al. [2008], Carlstrom et al. [2011]). During the 2007 to 2011 observing season the SPT conducted the SPT-SZ survey with the primary aims of measuring the CMB power spectrum to high l and detecting galaxy clusters via the SZE. The SPT-SZ survey covers roughly 2500 sq. deg. of the southern sky at frequencies of 90, 150 and 220 GHz. The final survey depths at each of these frequencies are roughly 40 μK-arcmin, 18 μK-arcmin, and 80 μK-arcmin respectively and the resolution of the maps is roughly 1 arcminute.

SPT records sky observations as a sequence of time-ordered data (TOD) while the telescope scans across the sky. Several filters are applied to the TOD to improve data quality and reduce computational overhead. These filters translate into a complicated, non-isotropic weighting pattern on the sky, i.e. the transfer function. Because of TOD filtering, the SPT transfer function departs significantly from isotropy; we must therefore consider the full, two-dimensional transfer function. The SPT-SZ Survey was divided into 19 fields across the full survey area. As different filtering schemes and scanning strategies were applied to different fields, the transfer function of SPT is field-dependent. Furthermore, the projection of data from the curved sky to flat maps causes the transfer function to vary slightly across

individual fields. Here, we ignore the intra-field variation of the transfer function, but do allow the transfer function to vary between fields. We use the transfer function measurements by George et al. in prep. [2014]. The optical response of the SPT to sources on the sky – the beam function – must also be characterized. Measurement of the beam function for SPT is described in Keisler et al. [2011]. The Fourier transform of the combined SPT 2D beam and transfer function – $B(\hat{n}, \hat{n'})$ in the notation introduced above – for a single field is shown in Fig. 3.1.

Instrumental noise in SPT is approximately white but there is some correlated noise structure. As the measurement of CMB cluster lensing relies on detecting small changes in correlations between pixels, it is important to build an accurate noise model for SPT data that takes these pixel correlations into account. The noise model can be built using SPT data itself. SPT generally performs a left and right scan for each field that it observes. While the sum of these two scans contains sky signal, the difference between the left and right scan maps should provide a measure of instrumental noise. The noise covariance matrix is calculated by sampling from these left-right difference maps[1]. In the sampling process we skip over patches of the sky that are near point sources or clusters. As with the transfer function, SPT's noise covariance is a field dependent quantity and we treat it as such in our analysis. The 2d noise covariance measured using the difference maps is shown in Fig. 3.2 for a single field.

SPT detects clusters via the SZE [e.g. Staniszewski et al., 2009]. To date, several hundred clusters have been found in the SPT-SZ survey. As the SZE is redshift independent, the SZE detection cannot be used to constrain the cluster redshift. Instead, redshifts of SZE-detected clusters are obtained via follow-up optical observations. A preliminary catalog of clusters detected at greater than 4.5σ significance with measured redshifts contains 523 clusters. For our analysis of mock data we assume the same number of clusters.

1. Since our method of eliminating SZE contamination involves the creation of a new, SZE-free map from a linear combination of three frequency maps, the left and right maps are also transformed via this linear combination before the noise covariance is computed.

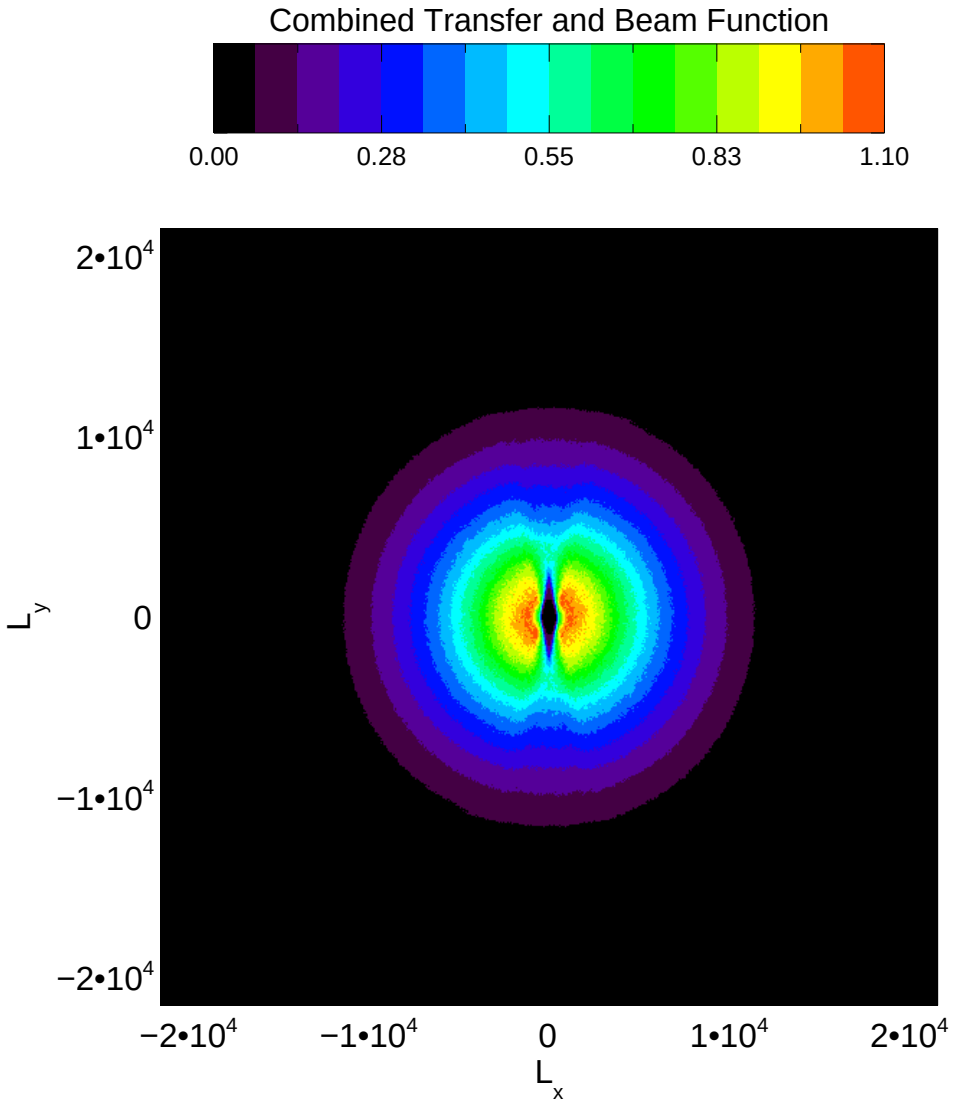

Figure 3.1: Combined l-space beam and transfer function for SPT field RA6HDEC-62.5.

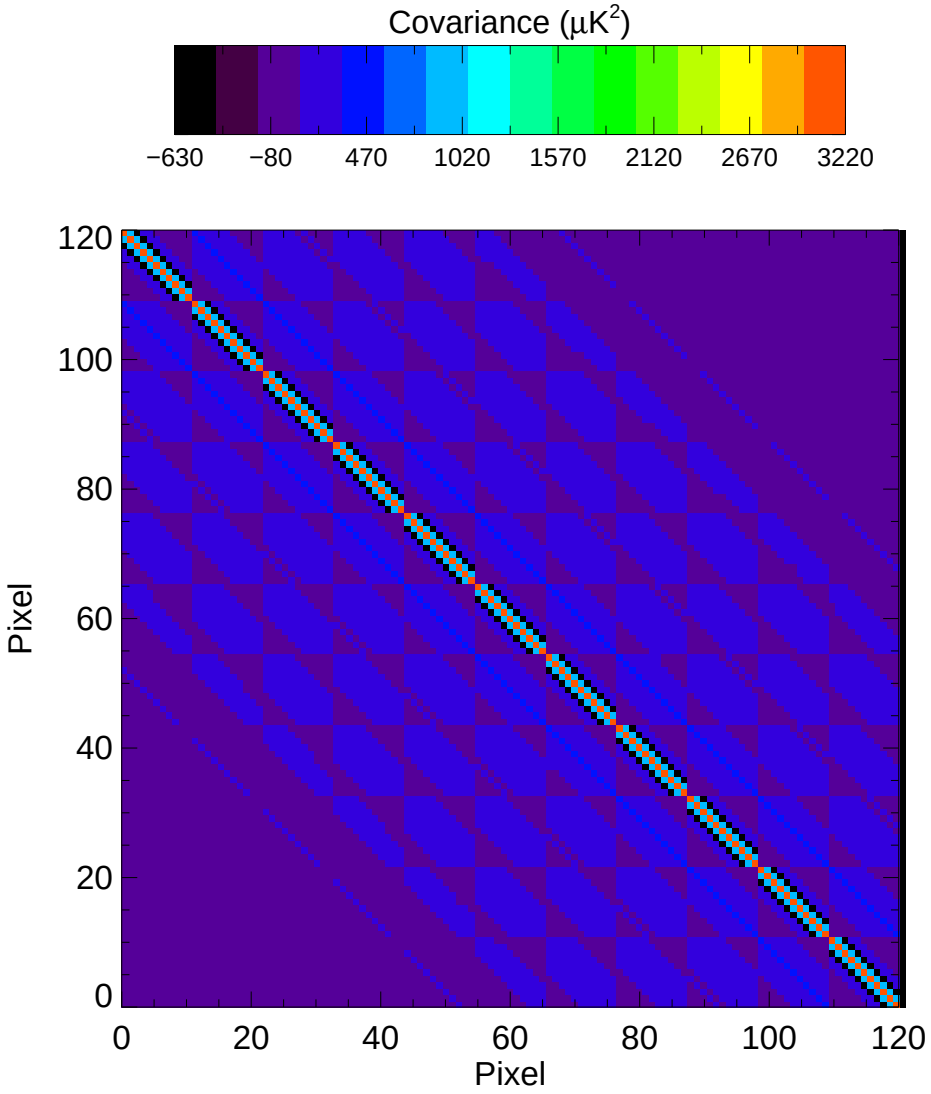

Figure 3.2: Noise covariance for SPT field RA6HDEC-62.5. While the noise covariance is mostly diagonal, there is significant off-diagonal structure. The 121 pixels are arranged in an 11×11 grid.

3.2 Generation of Mock Data

There are several steps to the generation of the mock data, each of which are described in detail below. The ultimate aim here is to generate a cutout of mock data around each mock cluster that is as close as possible to real data from the SPT. In most of our analysis we consider square cutouts that measure 5.5 arcminutes on a side, with square pixels 0.5 arcminutes on a side. This window is expected to contain the bulk of the CMB cluster lensing signal [e.g. Holder and Kosowsky, 2004], but extensions to large angular scales may be investigated in future work.

We first generate realizations of the CMB and foregrounds at 0.05 arcminute resolution (well below the final 0.5 arcminute pixel scale of the mocks) that are 70 arcmin on a side. The fine resolution is necessary to accurately capture the small deflections due to lensing, which are typically less than 0.5 arcminutes. The large window size (70 arcmin) relative to the final window size (5 arcmin) is necessary to correctly take into account the full effects of the beam and transfer function which have support out to large scales.

To generate the CMB realizations, we compute the unlensed pixel-pixel covariance matrix, C^{unlen}, at 1 arcminute resolution (Eq. 2.10). A Gaussian realization of C^{unlen} is then generated in the following manner. First, we compute the Cholesky decomposition of C^{unlen}:

$$C^{unlen} = SS^T \tag{3.1}$$

where S is a lower left triangular matrix. The existence of S is guaranteed by the fact that C^{unlen} is necessarily positive definite; there are several fast routines available for numerically computing the Cholesky decomposition. We then generate an N_{pix}-element vector $\vec{n}$ that consists of random numbers independently drawn from a normal distribution with unit variance. Computing $\vec{x} = S\vec{n}$ gives us the desired Gaussian random realization of C^{unlen}.

This can be confirmed by computing

$$\begin{aligned} cov(\vec{x},\vec{x}') &= E\left[S\vec{n}(S\vec{n}')^T\right] \\ &= E\left[S\vec{n}\vec{n}^T S^T\right] \\ &= SIS^T \\ &= C^{unlen}. \end{aligned}$$

To generate the high-resolution unlensed CMB map (0.05 arcminute resolution), we interpolate the low-resolution CMB map (1 arcminute resolution) generated from the covariance matrix. The CMB is very smooth below scales of ~ 10 arcminutes, so our interpolation from 1 arcminutes to smaller scales is justified.

We must also generate unlensed realizations of the foregrounds. The procedure described above is not feasible for the foregrounds since the foregrounds have most of their power at very small scales. This would entail a prohibitively large C^{unlen}. Instead, realizations of the foregrounds are generated starting with a realization of Gaussian white noise with unit variance at the high-resolution pixel scale. Fourier transforming this white noise map, multiplying by the desired power spectrum and Fourier transforming back gives us a map with the desired properties. Note that this method does not capture power at scales larger than 70 arcminutes (the size of the realization), hence our decision to use a different method for generating the CMB realizations. At scales larger than 70 arcminutes, however, the foreground power is dwarfed by the primordial CMB so this method is sufficient for generating foreground realizations.

With the unlensed CMB and foreground realizations generated, the next step is to compute the deflection angles across the high-resolution map. The deflection angles are computed using the NFW template from Eq. 1.8, assuming values of M_{200}, $z_{cluster}$, z_S, and c. Note that $z_S = 1089$ for the CMB, but as described previously, there is no single z_S for the foregrounds; our approach to dealing with this issue is discussed below. For our analysis we will

fix $c = 3$. While the true cluster profile may not be perfectly described by an NFW profile with $c = 3$, this is largely irrelevant to our aims here. We are interested in whether or not the analysis extracts the correct input model. Any failings of the NFW profile to fit true clusters is a more generic problem that is outside the scope of this work.

At this point it is important to again emphasize the distinction between the deflection field, $\delta(\vec{\theta})$, and the NFW deflection profile expressed as $D(\vec{\theta})$; the former takes photons observed at $\vec{\theta}$ to their unlensed positions, while the later takes photons originating from $\vec{\theta}$ to $\vec{\theta} + D(\vec{\theta})$. Since $D(\vec{\theta})$ is rotationally invariant and the deflection vectors always point in the radial direction, we compute $D(\vec{\theta})$ as a function of $|\vec{\theta}|$ and interpolate this function at the lensed positions to get $\delta(\vec{\theta})$.

Given a deflection field $\delta(\vec{\theta})$, the value of the lensed map at $\vec{\theta}$ is then computed by interpolating the unlensed map at $\vec{\theta} - \delta(\vec{\theta})$. This procedure is well defined as long as the fluctuations in the unlensed map are well-sampled; if, on the other hand, there are fluctuations in the map below the pixel scale (0.05 arcminutes for the high resolution map), then interpolating the map at new pixel positions will yield nonsensical results. Both the CMB and the clustered foreground meet this requirement: the primordial CMB is smooth over scales of about 10 arcminutes and the clustered foreground becomes subdominant to the other components at about 2 arcminutes. The Poisson foreground, however, is not well sampled in the unlensed map because it has power down to very small scales. To get around this, we generate a realization of the lensed Poisson foreground directly from the covariance matrix in Eq. 2.20. This realization is computed at the final pixel scale (0.5 arcminutes).

Next, the mock data are binned to 0.5 arcminutes to match the resolution at which the SPT beam and transfer function were computed. The beam and transfer function are then applied via Fourier space multiplication and a 5.5 arcminute window around the cluster center is then extracted (our final cutouts have 11×11 pixels, with the cluster occupying the central pixel). Finally, a realizations of the instrumental noise is generated from the measured noise covariance matrix and added to the mock data.

To generate an SPT-like catalog of cluster masses and redshifts we use the N-body simulations described in van Engelen et al. [2014]. Since the SPT-SZ survey covers roughly 2500 deg^2 while the simulations fill an octant on the sky, clusters were randomly selected from the simulation with probability $2500/5156.62 \sim 0.48$. The most massive 523 clusters were then selected from this reduced set of clusters. In reality, SPT identifies clusters based on their observed SZE decrement; since the decrement increases with mass, our selection of the most massive clusters is a reasonable proxy for the true SPT selection. The distribution of cluster masses in the mock survey is shown in Fig. 3.3.

Fig. 3.4 shows cutouts of the lensed and unlensed CMB with and without the beam applied; to make the effects of gravitational lensing more obvious, here we consider lensing by a $M_{200} = 10^{16}\,\mathrm{M}_\odot$ cluster. The cluster – which is located at the center of the image – has $z = 1$ and an NFW mass distribution with $c = 3$. Comparing the upper two panels of Fig. 3.4 makes it clear that the effect of gravitational lensing is to magnify the CMB near to the cluster center. Even for a $M_{200} = 10^{16}\,\mathrm{M}_\odot$ cluster, though, the effect is relatively small. The lower panels in Fig. 3.4 show that the beam has a significant impact on the observed temperature pattern on the sky. Since most of the power in the CMB is at large scales, the beam acts as a high-pass filter to the roughly 1.5 arcminute beam size, and therefore reduces its overall power.

Fig. 3.5 shows cutouts of the mock Poisson and clustered foregrounds with and without the beam applied. These figures make it clear that the foregrounds have significantly more small-scale power than the CMB. As a result, for the foregrounds the beam acts as a low pass filter to the roughly 1.5 arcminute beam size.

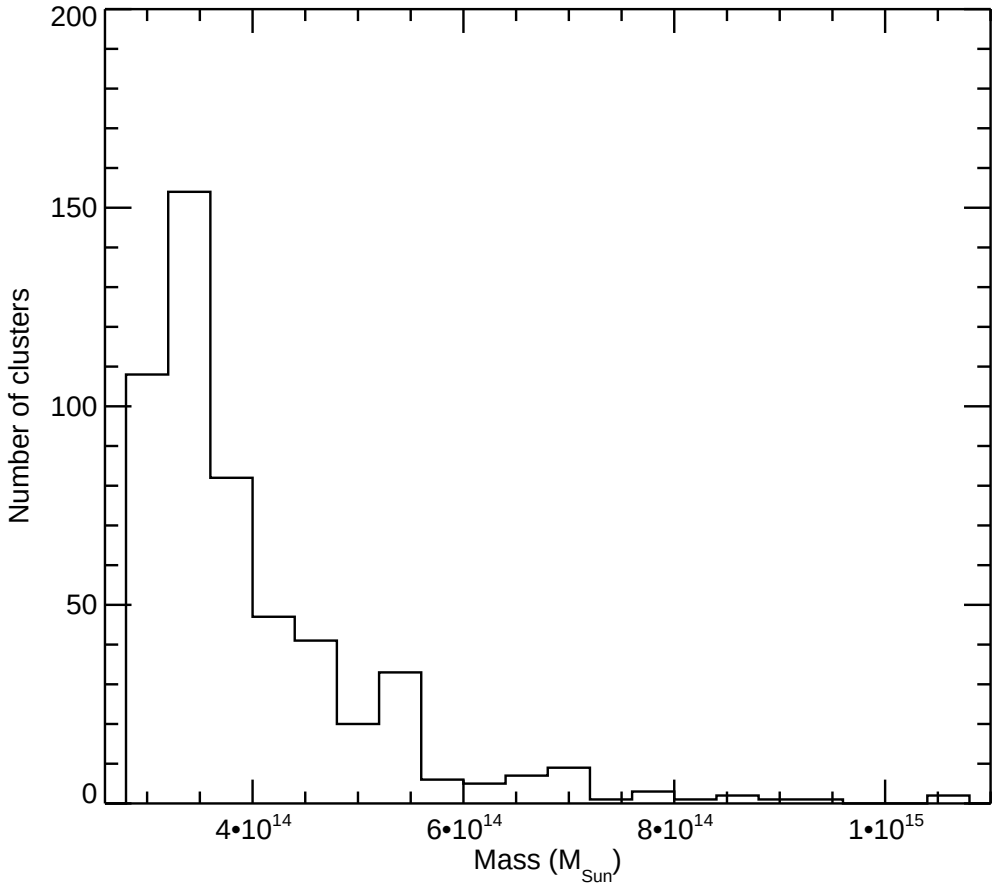

Figure 3.3: Distribution of cluster masses in the mock survey taken from the N-body simulations described in van Engelen et al. [2014].

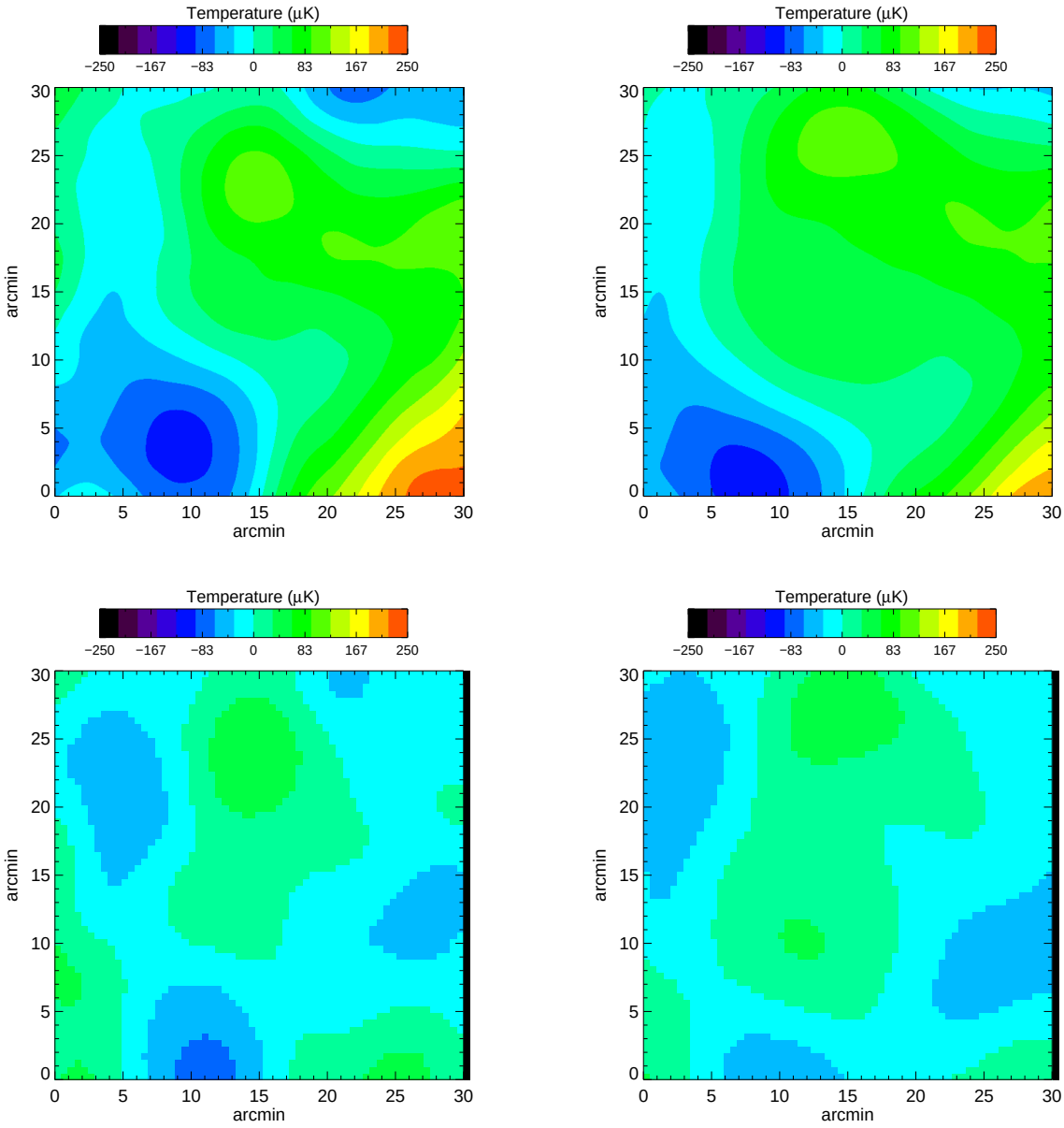

Figure 3.4: Cutouts from the mock data. Top left: unlensed CMB with no beam/transfer function; top right: lensed CMB with no beam/transfer function; lower left: unlensed CMB with beam/transfer function; bottom right: lensed CMB with beam/transfer function. To more clearly show the effects of gravitational lensing we assume a cluster mass of $M_{200} = 10^{16}\,\mathrm{M}_{\odot}$. The resolution of cutouts with the beam/transfer function has been degraded to the final pixel scale of 0.5 arcminutes.

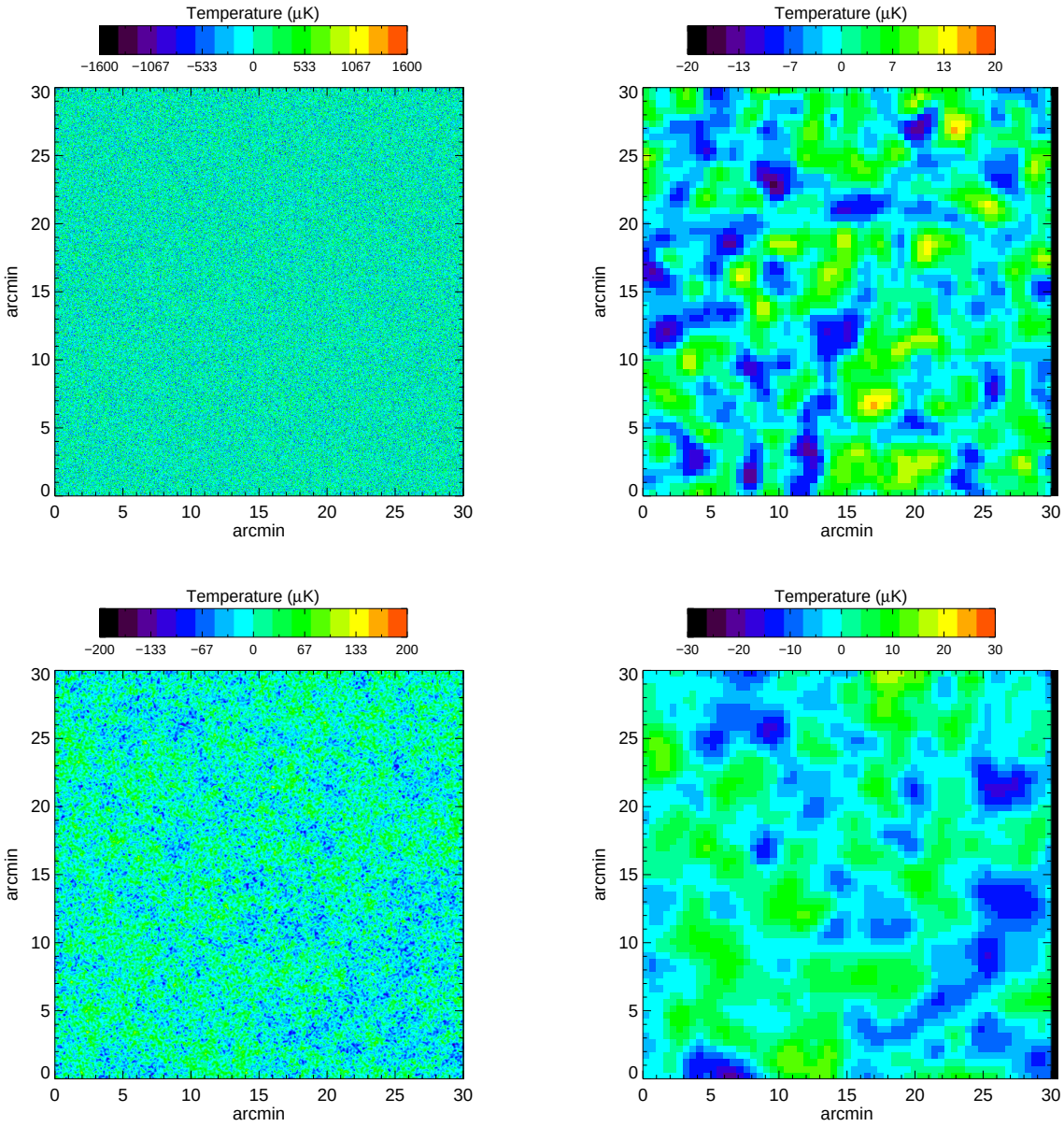

Figure 3.5: Cutouts from the mock data. Top left: unlensed Poisson foreground with no beam/transfer function; top right: unlensed Poisson foreground with beam/transfer function; lower left: unlensed clustering foreground with no beam/transfer function; bottom right: unlensed clustering foreground with beam/transfer function. The resolution of cutouts with the beam/transfer function has been degraded to the final pixel scale of 0.5 arcminutes.

CHAPTER 4

RESULTS OF ANALYSIS OF MOCK DATA

We now consider the results of analyzing the mock data described above. Our goal here is two-fold. First, we show that using the techniques presented above, the true cluster mass can be extracted with minimal bias; this is done by considering clusters of a single mass and redshift in a single field (i.e. single noise covariance, beam and transfer function). Second, we consider the analysis of a set of clusters with realistic masses and redshifts, to show the projected detection significance for data from the SPT-SZ survey. In both cases, we assume that the technique described above for eliminating SZE contamination has been applied (except when we consider the effects of SZE contamination in §4.2).

In order to establish the robustness of a detection of CMB cluster lensing, it is essential that we obtain no detection when the analysis is applied to the unlensed CMB. This null test ensures that if a lensing signal is observed, it is actually coming from *lensing*. In the mock data it is easy to simply turn off lensing. In the real data, this test can be performed by analyzing random patches of the CMB that are not near to clusters. Below, we show both the results of the null test ('Off cluster') as well as the results of the 'On cluster' analysis.

4.1 Single Field, Single Mass, Single Redshift

Fig. 4.1 shows the results of our analysis applied to mock data generated entirely from the CMB, without foregrounds or instrumental noise. We consider here clusters with $z = 1$, $M = 5 \times 10^{15}\,\mathrm{M}_{\odot}$ and concentration $c = 3$. The beam and transfer functions are those corresponding to SPT field RA6HDEC-62.5, which was chosen as representative of the other fields. Each dashed black curve corresponds to the likelihood computed from the data for a single mock cluster. We see that even in this highly idealized no-noise and no-foreground scenario, the lensing signal from a single cluster may not always be detected. This is because the ability to detect the signal depends on the behavior of the CMB behind the cluster: if

the CMB gradient behind the cluster is small, the CMB cluster lensing signal will also be small. On the other hand, if there is a large gradient behind a massive cluster, it may be possible to detect the lensing signal for a single cluster. The dashed curves in Fig. 4.1 also make it clear that the constraints on M_{200} for a single cluster are highly non-Gaussian. As a consequence of the central limit theorem, with many stacked clusters the constraints become more Gaussian.

The solid black curves in Fig. 4.1 corresponds to the combined likelihood from 523 clusters (since the true SPT sample has this many clusters) and the different curves are different realizations of the CMB for each of these 523 clusters. The solid blue curve is the combined constraint from all realizations of all clusters. It is clear from Fig. 4.1 that when the only source of sky signal is the lensed CMB, we recover the correct cluster mass with no measurable bias. Furthermore, we correctly recover $M = 0$ in the 'off cluster' case as expected.

Fig. 4.2 adds in the effects of unlensed foregrounds, both Poisson and clustered. These constitute an additional source of noise to the CMB cluster lensing measurement, so it is not surprising that the likelihood is broader in this case. It is interesting to note that the noise added by the foregrounds is large enough that detection of the cluster lensing effect for a single $M = 5 \times 10^{14}\,\mathrm{M}_\odot$ cluster is unlikely. The stacked constraint from 523 clusters is strong enough, though, to yield a many-σ detection. Again, we see that the true cluster mass is recovered with essentially no bias, and that $M = 0$ is recovered off-cluster.

Fig. 4.3 adds in the effects of instrumental noise. Comparing to Fig. 4.2, it is clear that instrumental noise significantly degrades our ability to constrain CMB cluster lensing. This is not unexpected since the level of instrumental noise is well above the magnitude of the cluster lensing signal for a single cluster. Detection of cluster lensing for a single $M = 5 \times 10^{14}\,\mathrm{M}_\odot$ cluster is impossible in this case. Again, though, we see that there is no apparent bias to the stacked results, on- or off cluster. It is also exciting to see that a detection of the cluster lensing effect is highly likely for 523 stacked clusters. We also note

that the shape of the likelihood is not invariant under shifts in M_{200}; the likelihood generally becomes narrower as $M_{200} \to 0$. This is not too surprising, as it is clear from Eq. 1.8 that the deflection angle scales roughly with $M_{200}/r_{200} \propto M^{2/3}$ (ignoring the dependence of $g(x)$ on the mass). Thus, at small mass, constant shifts in mass correspond to larger fractional changes in deflection angle.

4.2 The Effects of Contamination from the SZE

The SZE results in an increment or decrement (depending on the frequency of observation) in the CMB at the locations of galaxy clusters. As discussed previously, the magnitude of this effect can be well in excess of the CMB cluster lensing signal. We explore the effects of this contamination on our analysis by introducing an artificial SZE into our mock data. We construct the mock SZE signal by integrating Eq. 1.12 using the pressure profile given in Eq. 1.13. As above, we assume a NFW cluster with $M_{200} = 5 \times 10^{14}\,\mathrm{M}_{\odot}$, $z = 1$ and $c = 3$. The mock SZE signal is introduced into the mock data at high resolution and prior to the application of the beam.

Fig. 4.4 shows the effect of the mock SZE on our likelihood analysis. For this figure we include contributions from both Poisson and clustered foregrounds, as well as instrumental noise. Even though the shape of the SZE on the sky differs significantly from the cluster lensing signal, Fig. 4.4 makes it clear that the SZE significantly impacts the likelihood analysis. Simply ignoring the SZE leads to a very large bias in the lensing constraints on M_{200}. This is somewhat surprising given the very different morphologies of the SZE and cluster lensing signals. Apparently, the difference in morphology is not sufficient to prevent our analysis from being contaminated by the SZE. This motivates our decision to remove SZE contamination using frequency information as discussed above.

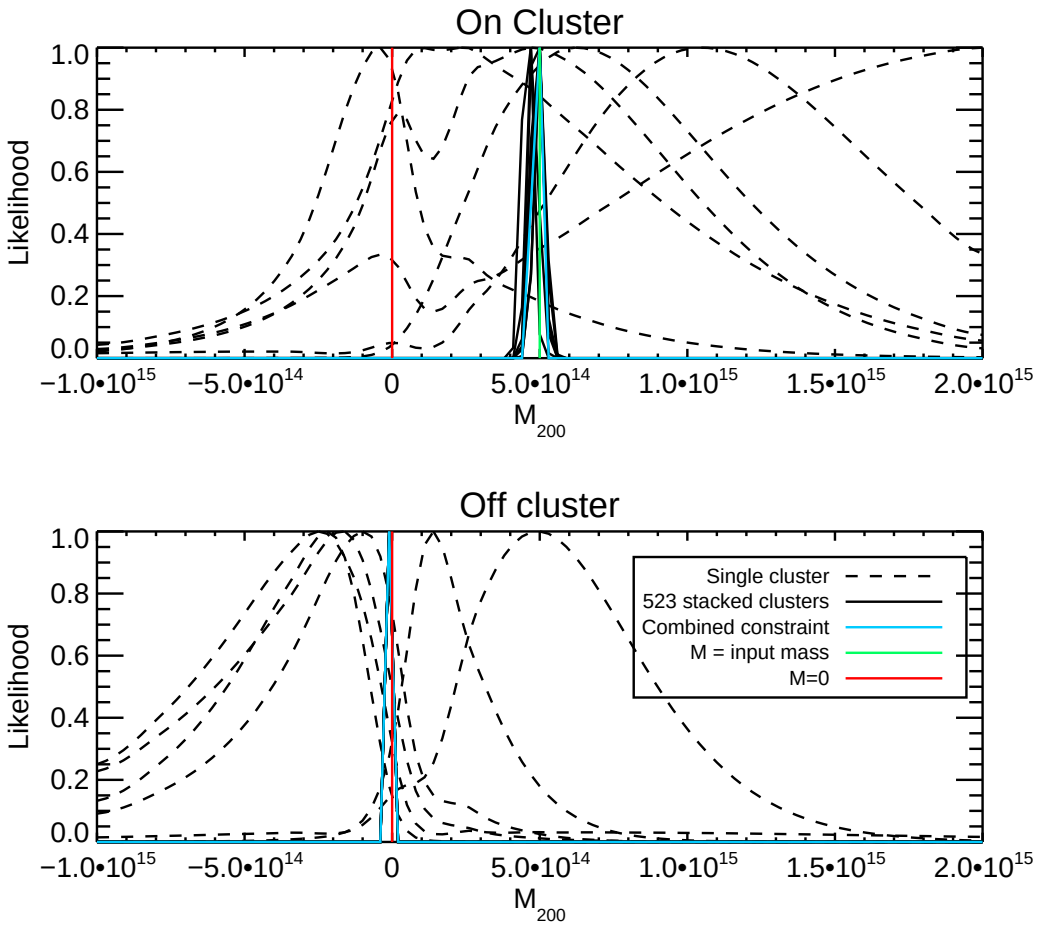

Figure 4.1: Likelihood constraints on M_{200} resulting from our analysis of mock data. The mock data analyzed for in this figure contains only lensed CMB (i.e. there is no instrumental noise or foreground contributions). The input cluster mass is $M_{200} = 5 \times 10^{14} M_{odot}$, shown as the vertical green line. Each black curve represents the combined likelihood from 523 mock clusters; the different black curves correspond to different realizations of the CMB behind these clusters. The blue curve is the combined constraint from all clusters and all CMB realizations.

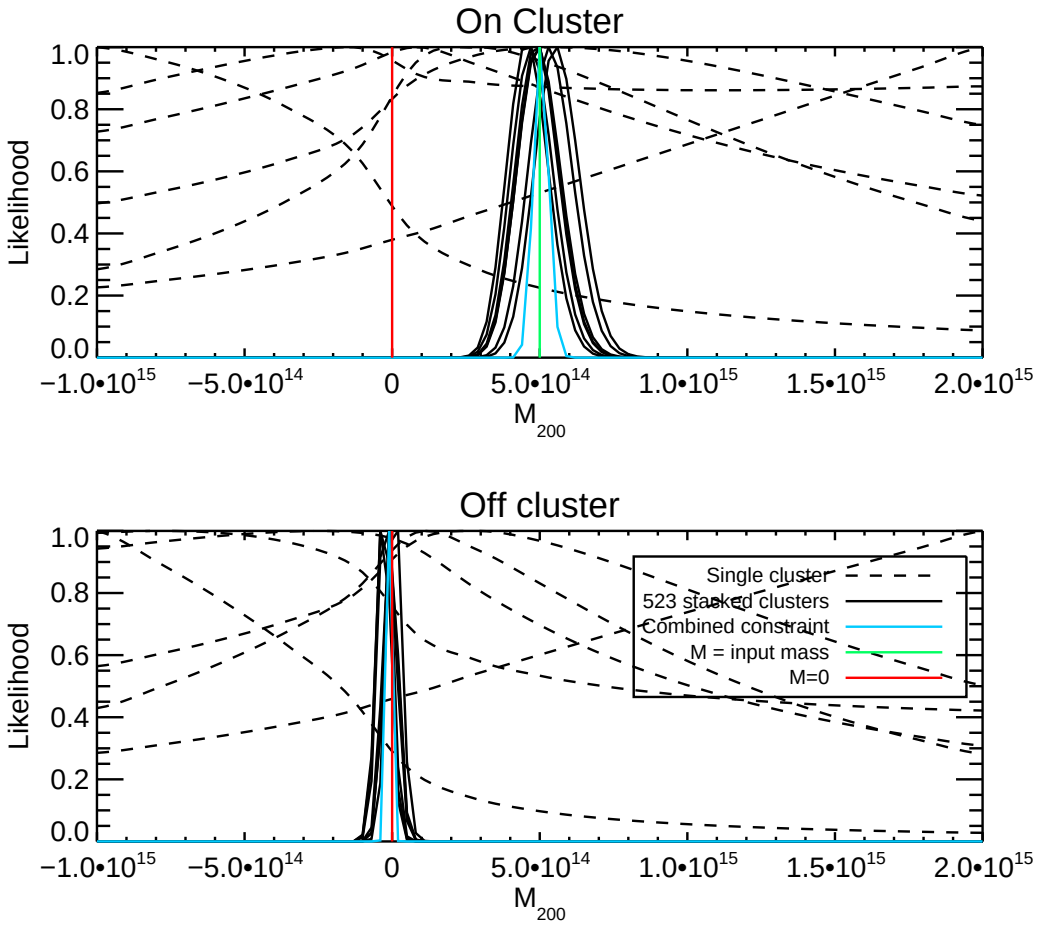

Figure 4.2: Same as Fig. 4.1 except that now unlensed foregrounds (both Poisson and clustered) have been added to the mock data.

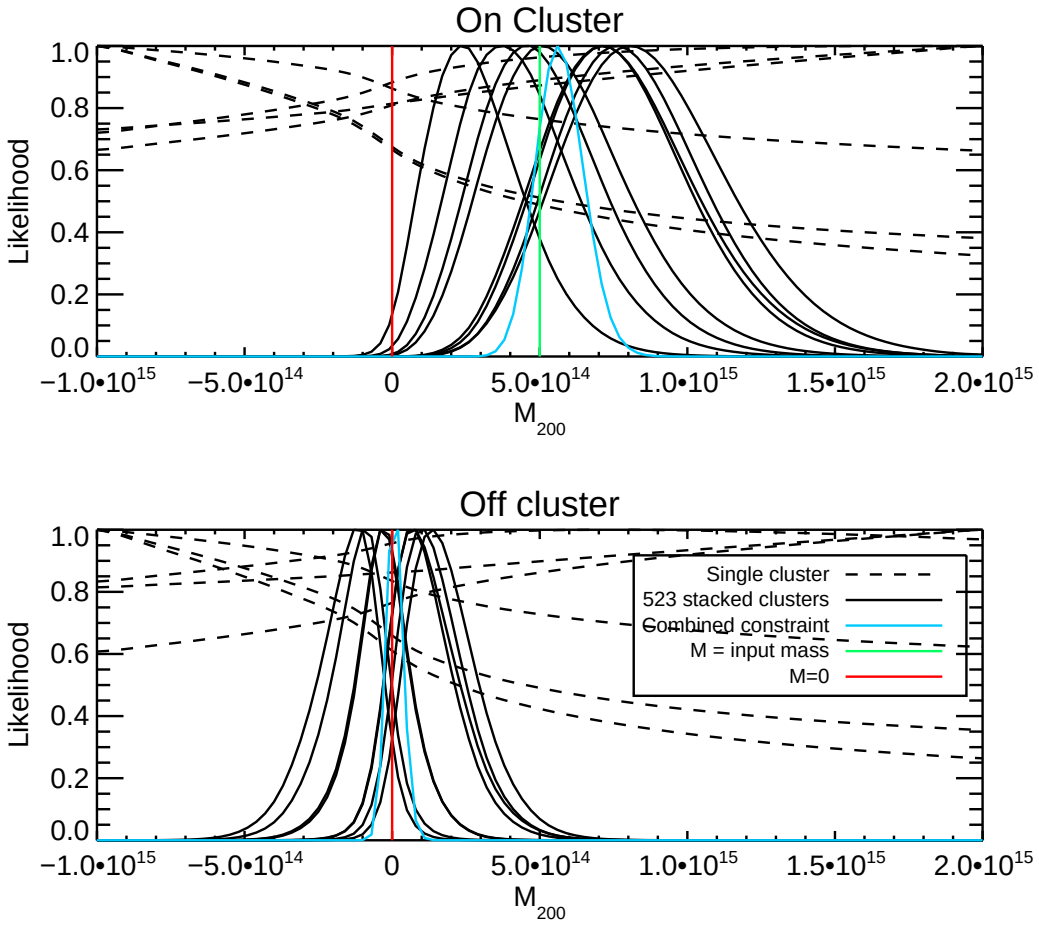

Figure 4.3: Same as Fig. 4.2 except that now instrumental noise has been added to the mock data.

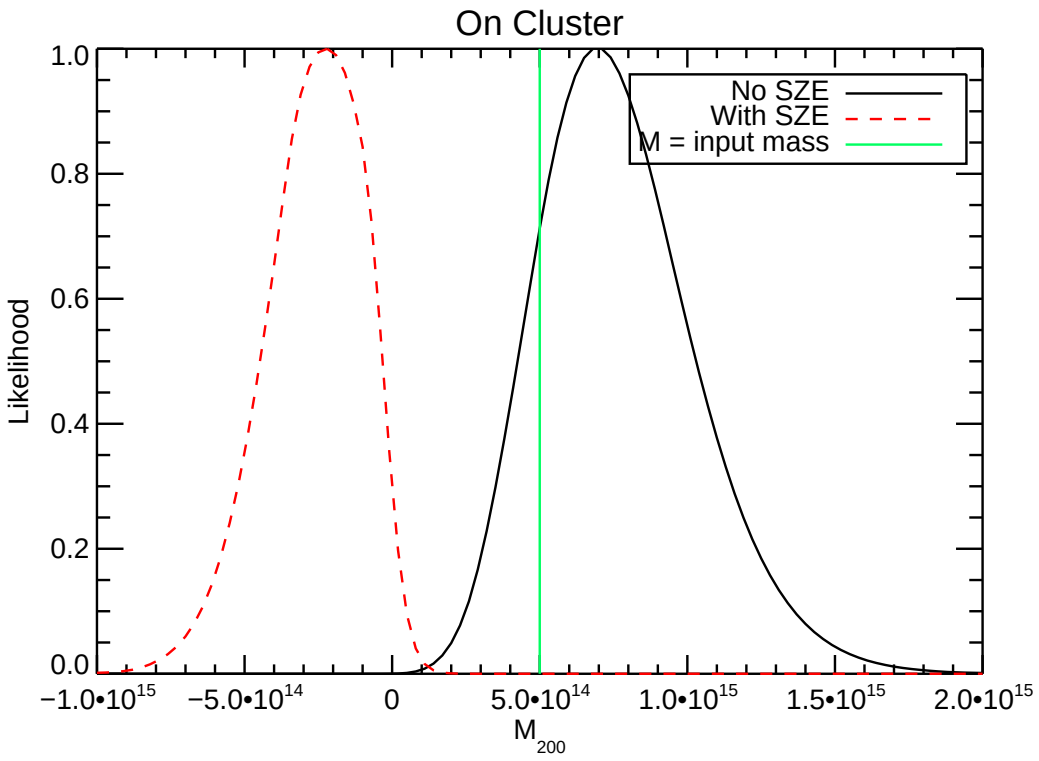

Figure 4.4: The impact of the SZE on the detection of CMB cluster lensing. Simply ignoring the SZE in our analysis causes us to reject the true cluster mass (and to prefer a negative mass) at high significance.

4.3 Lensing of the Foregrounds

As discussed in §1.6, the degree to which Poisson and clustered foreground emission will be lensed by the cluster is not very well constrained. The CIB is thought to originate from redshifts $z \sim 0.5$ to 4; since our cluster sample has $z \sim 0.1$ to 1, the amount of lensing that the foregrounds experience will likely vary from cluster to cluster. Fig. 4.5 shows how the diagonal elements of the Poisson covariance matrix change with gravitational lensing depending on the redshift from which the foreground originates. As described above, we consider an 11×11 pixel window around the cluster, so that $N_{pix} = 121$ and pixel 60 is on the cluster center. The effects of lensing on the Poisson covariance matrix are computed by directly integrating Eq. 2.20. From Fig. 4.5 it is clear that lensing can significantly alter the Poisson covariance matrix, changing the variance of pixels near the cluster center by a factor of ~ 2 (this is consistent with e.g. Hezaveh et al. [2013]). It is also clear that the covariance matrix changes more for larger foreground redshift. This is a simple consequence of Eq. 1.7: the deflection angles increase with increasing source redshift.

To investigate the effects of cluster lensing of the foregrounds on our analysis, we consider two extremes: no lensing of the foregrounds, and lensing of the foregrounds assuming foreground emission originates from $z = 4$. We have already considered the case of no foreground lensing above. Since the CIB is not expected to have significant contributions from $z > 4$, setting $z = 4$ gives an upper bound to the effects of gravitational lensing on the foregrounds. We generate lensed realizations of the foregrounds using the techniques discussed in §3.2. Since the clustering foreground has little small-scale power, we can simply interpolate an unlensed map of this foreground at the lensed positions. This is not possible for the Poisson foreground (since it has very small scale power), so we instead directly generate realizations of the lensed Poisson covariance matrix.

The results of analyzing mock data with lensed foreground emission originating from $z = 4$ are shown in Fig. 4.6. We emphasize that the *analysis* still assumes that the foregrounds are unlensed. The top panel considers the effects of lensing of the Poisson foreground

only (with no clustered foreground), the middle panel considers the effects of lensing of the clustered foreground (with no Poisson foreground) and the bottom panel considers the effects of lensing both foregrounds. In each panel, the curves represent a stacked constraint from 24 realizations of 523 mock clusters. Apparently, lensing of the Poisson foreground at this level causes the M_{200} constraint to be biased high by $\sim 10\%$. This is not too surprising as lensing of the Poisson foreground induces changes to the covariance structure of the data that are not accounted for in the model; these changes are similar to those induced by CMB lensing, and so the best fit M_{200} shifts up. Lensing of the clustered foreground, on the other hand, apparently has little effect on our CMB lensing constraints. The net result of lensing of both foregrounds is a roughly 10% shift of our lensing constraint to higher mass. Since this shift is well below the statistical error bars associated with the cluster lensing constraints presented here, we ignore this effect below.

4.4 Multiple fields, Multiple Masses, Multiple redshifts

Now we consider the analysis of more realistic mock data for which the cluster masses and redshifts are designed to approximate those in the SPT-SZ survey (see §4.2). Further, we allow the noise covariance, beam and transfer function to vary between clusters as it does in the SPT-SZ survey due to the clusters residing in different fields. Having already addressed the various systematics that may affect the CMB cluster lensing measurement, we restrict our attention here to unlensed foregrounds with no additional contaminants.

Fig. 4.7 shows the results of analyzing the realistic mock survey data. The range of cluster masses in the sample leads to a corresponding spread in the likelihood. Even with this spread, though, Fig. 4.7 suggests that we will likely obtain a detection of cluster lensing if our analysis assumes a single mass for the entire cluster sample. Since the likelihoods are moderately non-Gaussian, we evaluate the detection significance by compute the integrated probability of $M_{200} > 0$. Averaged over the different realizations of the full cluster sample, the projected detection significance is 3.9σ. We also see that the lensing constraint agrees

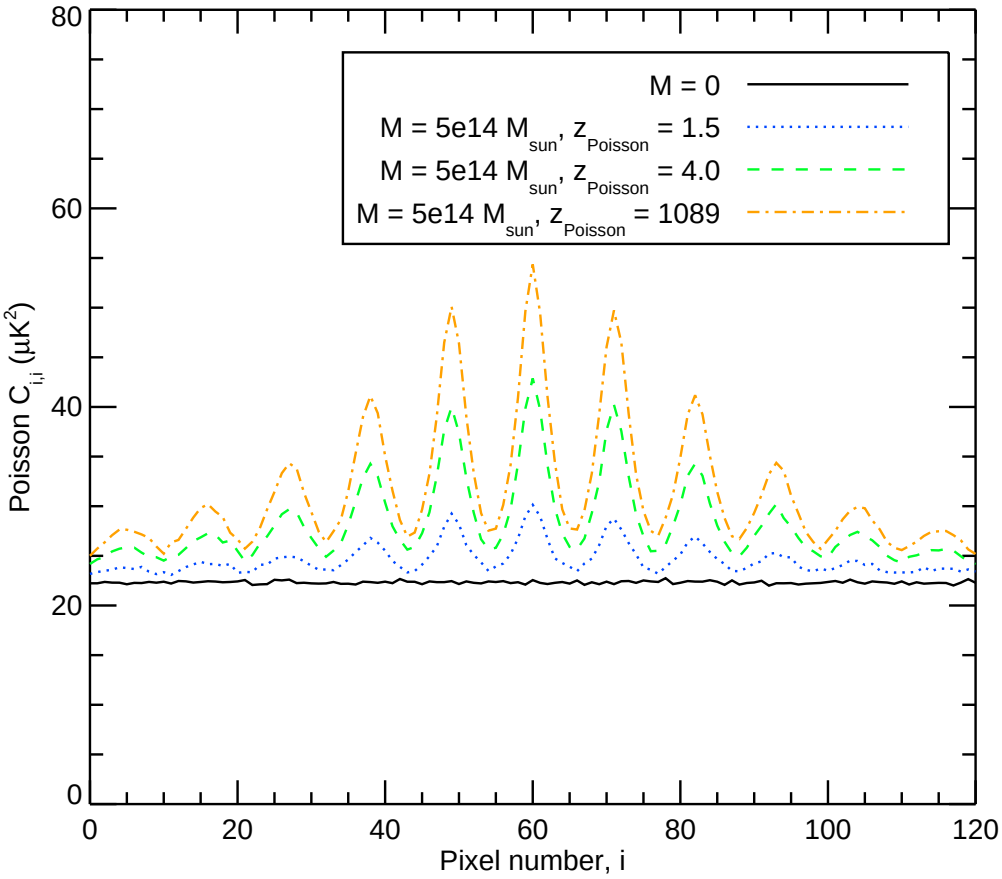

Figure 4.5: Effects of lensing on the Poisson covariance matrix, computed by direct integration of using Eq. 2.20. We consider here a cluster located at $z = 1$.

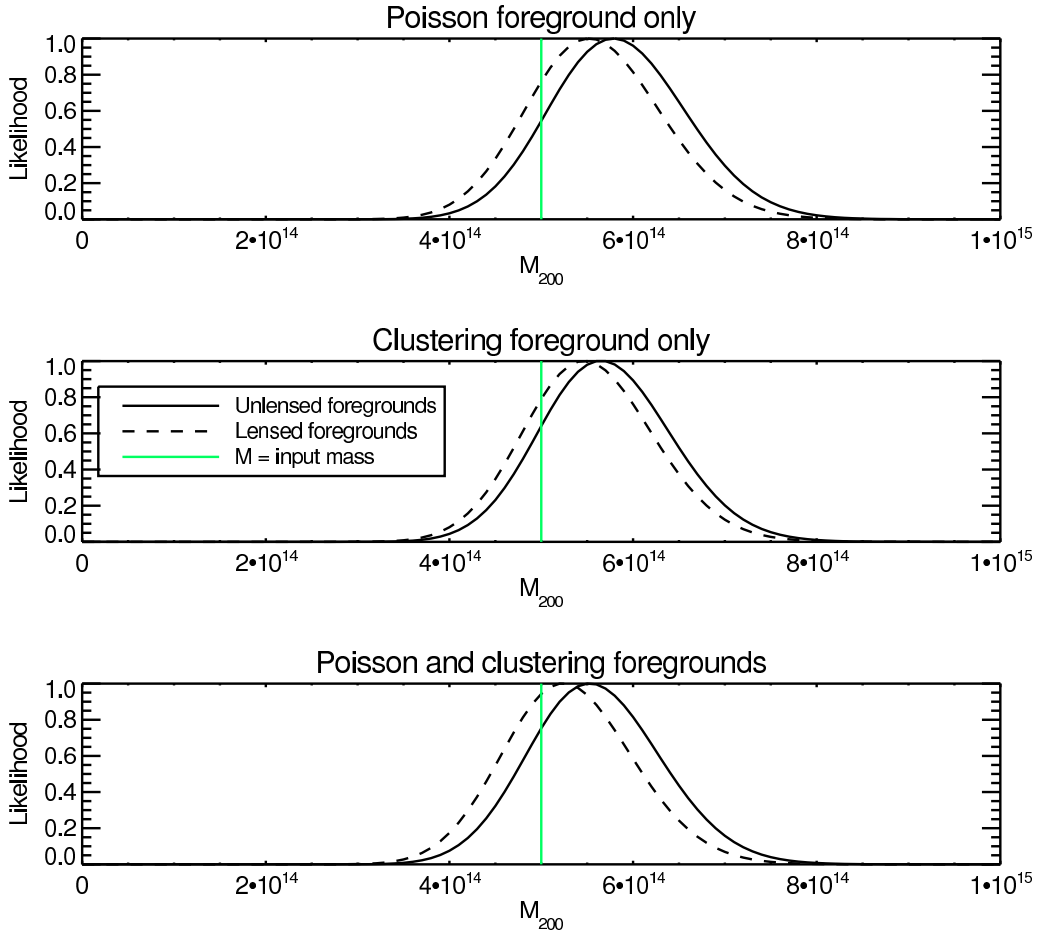

Figure 4.6: The effects of foreground lensing on the CMB cluster lensing likelihood constraints. The foreground emission is assumed to originate from $z = 4$, which should overestimate the effects of foreground lensing on the data. Each curve corresponds to the stacked likelihood of 24 realizations of 523 mock clusters that include lensed CMB and the indicated foreground. The lensed clustered foreground maps are generated using the simulation technique described in §3.2; the lensed Poisson maps are generated using the technique described in §4.3. It is apparent from the figure that lensing of the Poisson foreground leads to a less than 10% bias in our analysis. The effect is overestimated here as most of the Poisson foreground emission comes from $z < 4$.

well with the average mass of the cluster sample in our mocks (the vertical purple line).

As discussed in §2.6, one way to account for the spread in cluster masses is to evaluate the likelihood as a function of $M_{200}/M_{\mathrm{external},i}$, where $M_{\mathrm{external},i}$ is some mass proxy for the ith cluster. In the actual data, $M_{\mathrm{external},i}$ could be derived, for example, from a scaling relation between some SZE observable and mass. In the mock data, since we know the true cluster mass, it makes sense to evaluate the likelihood as a function of M_{200}/M_{true}. These results are shown in Fig. 4.8; as expected the likelihood peaks at $M_{200}/M_{true} = 1$. Furthermore, these results show a slightly stronger detection of the cluster lensing effect than in Fig. 4.7 because the likelihood is not broadened by the spread in cluster mass. When the likelihood is evaluated in this way, the mean detection significance is 4.1σ.

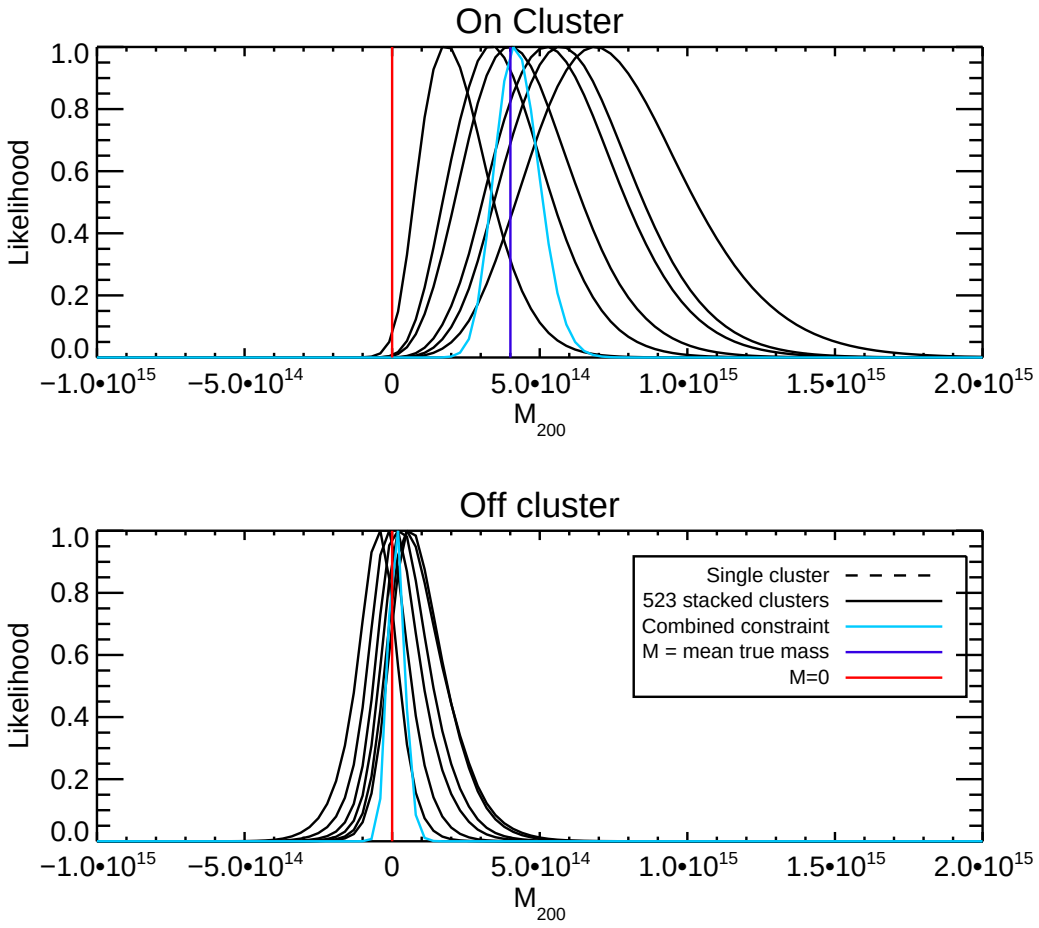

Figure 4.7: Constraints on M_{200} resulting from analysis of mock data designed to replicate as closely as possible data from the SPT. Each black curve corresponds to stacked constraints from an SPT-like survey that detects 523 clusters; the blue curves are combined constraints from six such surveys. The cluster mass and redshift distributions are dervied from the N-body simulations described in van Engelen et al. [2014]. The vertical purple line represents the mean mass of this sample; the full mass distribution is shown in Fig. 3.3.

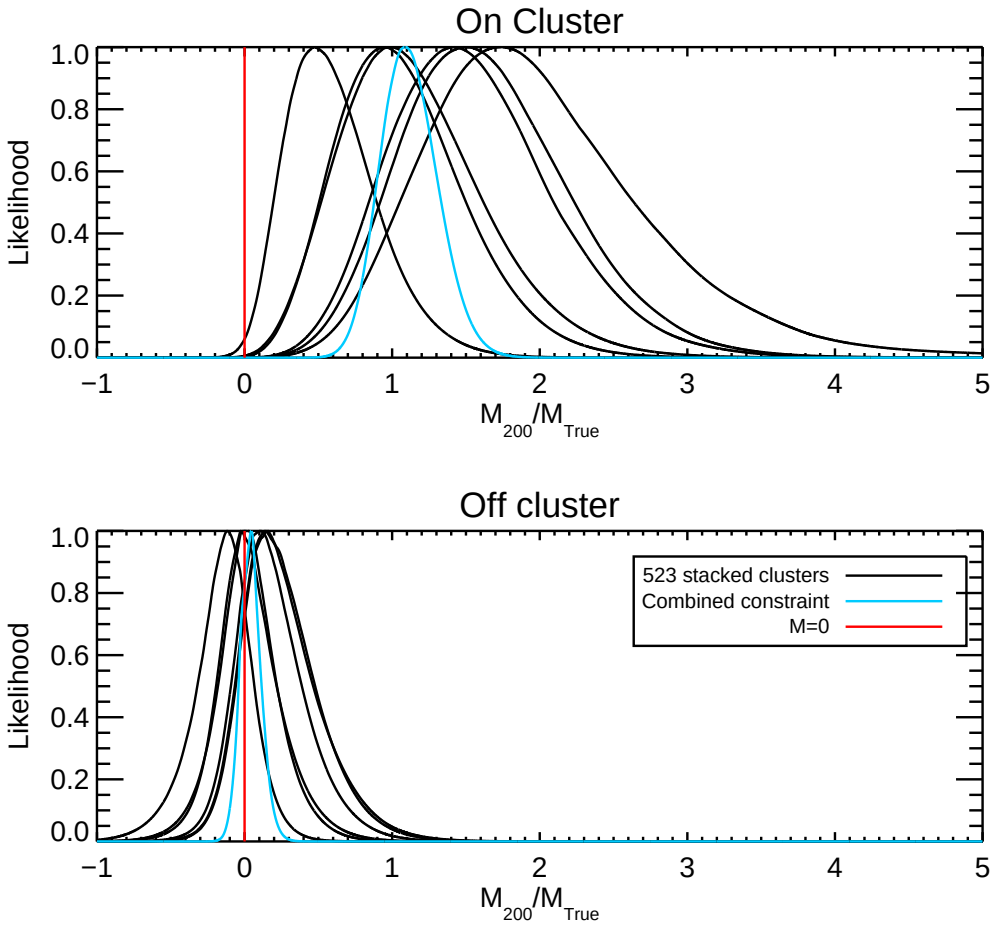

Figure 4.8: Same as Fig. 4.7 except that the likelihood for each cluster is now evaluated as a function of M_{200}/M_{true}, where M_{true} is the true cluster mass.

CHAPTER 5

CONCLUSION

Gravitational lensing of the CMB by galaxy clusters can potentially be used as a powerful probe of cluster mass. Improved constraints on cluster masses are in turn essential for the use of galaxy clusters as cosmological probes. To date, however, the CMB cluster lensing signal remains undetected. In this thesis we have developed a maximum likelihood approach to constraining the CMB cluster lensing signal and have applied this analysis to mock data designed to mimic real data from the SPT-SZ survey. We have considered two important potential sources of systematic error: contamination from the SZE and lensing of the foregrounds. The SZE is shown to lead to significant bias in the recovered mass constraints, but it can be removed with the use of frequency information. Lensing of the Poisson foreground leads to at most a 10% bias in the lensing mass constraints and can therefore be safely ignored in a first detection. With the analysis of mock data we have shown that the projected detection significance for SPT is at the 4σ level when the likelihood constraints are stacked across ~ 500 clusters.

The future of CMB cluster lensing is bright. The noise levels of currently available CMB data are significantly above the cluster lensing signal. Ongoing and future CMB experiments such as SPTPol [Bleem et al., 2012], ACTPol [Naess et al., 2014], SPT-3G [Benson et al., 2014] and so-called Stage IV CMB experiments [e.g. Abazajian et al., 2013] will have significantly lower noise levels than the SPT-SZ survey, allowing them to obtain significantly stronger detections of the CMB cluster lensing signal. Fig. 5.1 shows the projected measurement of the CMB cluster lensing signal in a SPT-3G-like survey that has noise levels of 4.2, 2.5, 4.0 μK-arcmin noise in the 90, 150 and 220 GHz channels, respectively. The SPT-3G curve shows the stacked constraint for 1250 clusters, normalized to the true cluster masses. Given its low noise levels, SPT-3G will likely have the ability to measure the CMB cluster lensing signal for some very massive individual clusters that are on top of large gradients in the CMB. The Stage IV goal of attaining $1\,\mu$K-arcmin depth over 50%

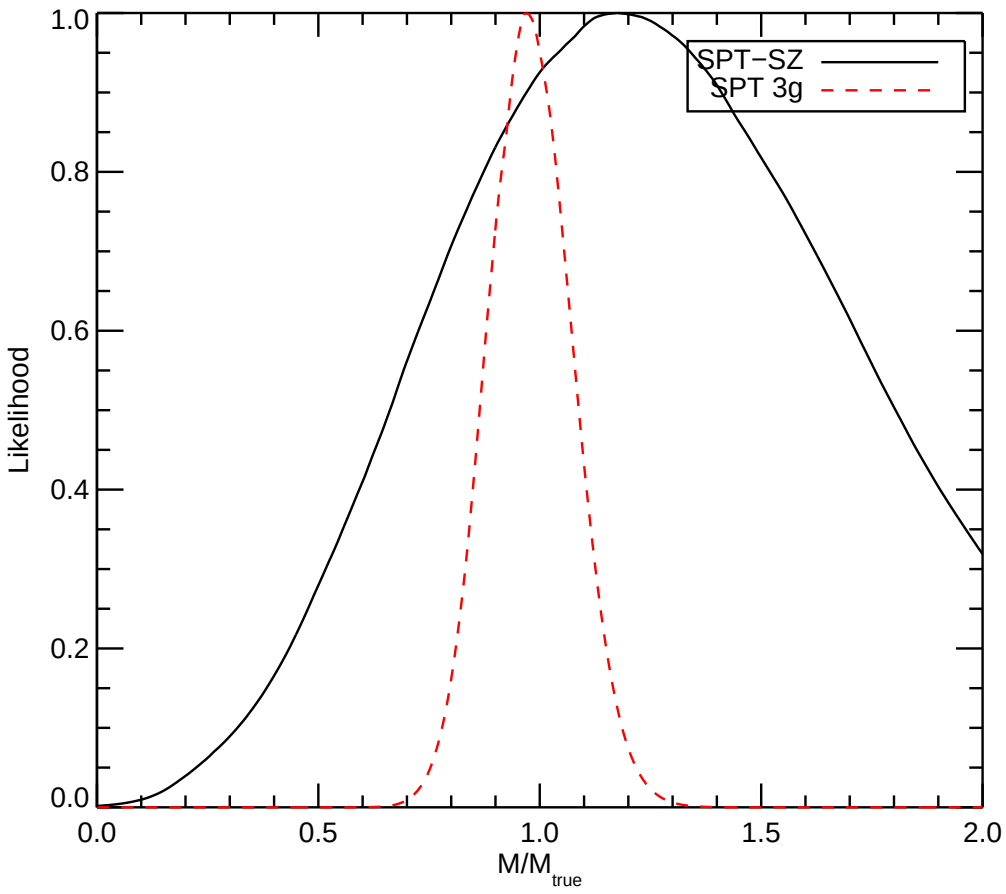

Figure 5.1: Projected constraints on the ratio of M_{lens}/M_{true} for the SPT-SZ survey and the SPT-3G survey.

of the sky would almost certainly enable study of the CMB cluster lensing effect for many individual clusters.

Another exciting improvement to CMB cluster lensing measurements offered by ongoing and future experiments is the addition of polarization information. Because correlation between temperature and polarization B modes, or between polarization E and B modes, is not expected to be present in the primordial CMB at small angular scales, these correlations offer a direct and high signal-to-noise measure of gravitational lensing [e.g. Hu and Okamoto, 2002]. In general then, polarization measurements should result in improved constraints on CMB lensing and in particular the cluster lensing signal. Furthermore, polarization offers

another handle on eliminating contamination from the SZE. The polarized SZE (both thermal and kinematic) from clusters is expected to be significantly smaller than the unpolarized effect, so polarization observations in principle offer a less-contaminated window into CMB cluster lensing [e.g. Holder and Kosowsky, 2004].

As the precision of CMB cluster lensing measurements improves, such measurements will become an essential tool for probing cluster masses. Early detections of the cluster lensing signal will likely be at the few sigma level, as we have seen above. Such measurements are very interesting, but they do not provide very much information on the cluster masses themselves. With higher quality data, CMB cluster lensing can provide powerful constraints on cluster masses. These mass constraints will serve several valuable purposes. First, they will provide a way of calibrating cluster masses detected via the SZE using CMB data alone. Second, these mass constraints can be used to improve cluster mass-observable relationships that are essential for using clusters as cosmological probes. Finally, because the systematics associated with CMB cluster lensing measurements are so different from those of other weak lensing measurements, CMB cluster lensing provides a cross-check on these measurements and a possible avenue for studying weak lensing systematics.

This work has addressed some of the important systematics for measurement of the CMB cluster lensing signal, including contamination from the thermal SZE and uncertainty in the redshift distribution of foreground emission. As discussed above, however, there are additional systematics that are deserving of more consideration, including residual thermal SZE contamination and kinematic SZE contamination. Future work will attempt to study the effects of these sources of contamination in more detail.

REFERENCES

K. N. Abazajian, K. Arnold, J. Austermann, B. A. Benson, C. Bischoff, J. Bock, J. R. Bond, J. Borrill, E. Calabrese, J. E. Carlstrom, C. S. Carvalho, C. L. Chang, H. C. Chiang, S. Church, A. Cooray, T. M. Crawford, K. S. Dawson, S. Das, M. J. Devlin, M. Dobbs, S. Dodelson, O. Dore, J. Dunkley, J. Errard, A. Fraisse, J. Gallicchio, N. W. Halverson, S. Hanany, S. R. Hildebrandt, A. Hincks, R. Hlozek, G. Holder, W. L. Holzapfel, K. Honscheid, W. Hu, J. Hubmayr, K. Irwin, W. C. Jones, M. Kamionkowski, B. Keating, R. Keisler, L. Knox, E. Komatsu, J. Kovac, C.-L. Kuo, C. Lawrence, A. T. Lee, E. Leitch, E. Linder, P. Lubin, J. McMahon, A. Miller, L. Newburgh, M. D. Niemack, H. Nguyen, H. T. Nguyen, L. Page, C. Pryke, C. L. Reichardt, J. E. Ruhl, N. Sehgal, U. Seljak, J. Sievers, E. Silverstein, A. Slosar, K. M. Smith, D. Spergel, S. T. Staggs, A. Stark, R. Stompor, A. G. Vieregg, G. Wang, S. Watson, E. J. Wollack, W. L. K. Wu, K. W. Yoon, and O. Zahn. Neutrino Physics from the Cosmic Microwave Background and Large Scale Structure. ArXiv e-prints, September 2013.

V. Acquaviva and C. Baccigalupi. Dark energy records in lensed cosmic microwave background. Phys. Rev. D, 74(10):103510, November 2006. doi: 10.1103/PhysRevD.74.103510.

A. Albrecht, G. Bernstein, R. Cahn, W. L. Freedman, J. Hewitt, W. Hu, J. Huth, M. Kamionkowski, E. W. Kolb, L. Knox, J. C. Mather, S. Staggs, and N. B. Suntzeff. Report of the Dark Energy Task Force. ArXiv Astrophysics e-prints, September 2006.

M. Arnaud, G. W. Pratt, R. Piffaretti, H. Böhringer, J. H. Croston, and E. Pointecouteau. The universal galaxy cluster pressure profile from a representative sample of nearby systems (REXCESS) and the Y_{SZ} - M_{500} relation. A&A, 517:A92, July 2010. doi: 10.1051/0004-6361/200913416.

B. A. Benson, P. A. R. Ade, Z. Ahmed, S. W. Allen, K. Arnold, J. E. Austermann, A. N. Bender, L. E. Bleem, J. E. Carlstrom, C. L. Chang, H. M. Cho, S. T. Ciocys, J. F. Cliche,

T. M. Crawford, A. Cukierman, T. de Haan, M. A. Dobbs, D. Dutcher, W. Everett, A. Gilbert, N. W. Halverson, D. Hanson, N. L. Harrington, K. Hattori, J. W. Henning, G. C. Hilton, G. P. Holder, W. L. Holzapfel, K. D. Irwin, R. Keisler, L. Knox, D. Kubik, C. L. Kuo, A. T. Lee, E. M. Leitch, D. Li, M. McDonald, S. S. Meyer, J. Montgomery, M. Myers, T. Natoli, H. Nguyen, V. Novosad, S. Padin, Z. Pan, J. Pearson, C. L. Reichardt, J. E. Ruhl, B. R. Saliwanchik, G. Simard, G. Smecher, J. T. Sayre, E. Shirokoff, A. A. Stark, K. Story, A. Suzuki, K. L. Thompson, C. Tucker, K. Vanderlinde, J. D. Vieira, A. Vikhlinin, G. Wang, V. Yefremenko, and K. W. Yoon. SPT-3G: A Next-Generation Cosmic Microwave Background Polarization Experiment on the South Pole Telescope. ArXiv e-prints, July 2014.

M. Béthermin, E. Le Floc'h, O. Ilbert, A. Conley, G. Lagache, A. Amblard, V. Arumugam, H. Aussel, S. Berta, J. Bock, A. Boselli, V. Buat, C. M. Casey, N. Castro-Rodríguez, A. Cava, D. L. Clements, A. Cooray, C. D. Dowell, S. Eales, D. Farrah, A. Franceschini, J. Glenn, M. Griffin, E. Hatziminaoglou, S. Heinis, E. Ibar, R. J. Ivison, J. S. Kartaltepe, L. Levenson, G. Magdis, L. Marchetti, G. Marsden, H. T. Nguyen, B. O'Halloran, S. J. Oliver, A. Omont, M. J. Page, P. Panuzzo, A. Papageorgiou, C. P. Pearson, I. Pérez-Fournon, M. Pohlen, D. Rigopoulou, I. G. Roseboom, M. Rowan-Robinson, M. Salvato, B. Schulz, D. Scott, N. Seymour, D. L. Shupe, A. J. Smith, M. Symeonidis, M. Trichas, K. E. Tugwell, M. Vaccari, I. Valtchanov, J. D. Vieira, M. Viero, L. Wang, C. K. Xu, and M. Zemcov. HerMES: deep number counts at 250 μm, 350 μm and 500 μm in the COSMOS and GOODS-N fields and the build-up of the cosmic infrared background. A&A, 542:A58, June 2012. doi: 10.1051/0004-6361/201118698.

M. Birkinshaw. The Sunyaev-Zel'dovich effect. Phys. Rep., 310:97–195, March 1999. doi: 10.1016/S0370-1573(98)00080-5.

A. Blanchard and J. Schneider. Gravitational lensing effect on the fluctuations of the cosmic background radiation. A&A, 184:1–6, October 1987.

L. Bleem, P. Ade, K. Aird, J. Austermann, J. Beall, D. Becker, B. Benson, J. Britton, J. Carlstrom, C. L. Chang, H. Cho, T. de Haan, T. Crawford, A. Crites, A. Datesman, M. Dobbs, W. Everett, A. Ewall-Wice, E. George, N. Halverson, N. Harrington, J. Henning, G. Hilton, W. Holzapfel, S. Hoover, J. Hubmayr, K. Irwin, R. Keisler, J. Kennedy, A. Lee, E. Leitch, D. Li, M. Lueker, D. P. Marrone, J. McMahon, J. Mehl, S. Meyer, J. Montgomery, T. Montroy, T. Natoli, J. Nibarger, M. Niemack, V. Novosad, S. Padin, C. Pryke, C. Reichardt, J. Ruhl, B. Saliwanchik, J. Sayre, K. Schafer, E. Shirokoff, K. Story, K. Vanderlinde, J. Vieira, G. Wang, R. Williamson, V. Yefremenko, K. W. Yoon, and E. Young. An Overview of the SPTpol Experiment. Journal of Low Temperature Physics, 167:859–864, June 2012. doi: 10.1007/s10909-012-0505-y.

J. E. Carlstrom, P. A. R. Ade, K. A. Aird, B. A. Benson, L. E. Bleem, S. Busetti, C. L. Chang, E. Chauvin, H.-M. Cho, T. M. Crawford, A. T. Crites, M. A. Dobbs, N. W. Halverson, S. Heimsath, W. L. Holzapfel, J. D. Hrubes, M. Joy, R. Keisler, T. M. Lanting, A. T. Lee, E. M. Leitch, J. Leong, W. Lu, M. Lueker, D. Luong-van, J. J. McMahon, J. Mehl, S. S. Meyer, J. J. Mohr, T. E. Montroy, S. Padin, T. Plagge, C. Pryke, J. E. Ruhl, K. K. Schaffer, D. Schwan, E. Shirokoff, H. G. Spieler, Z. Staniszewski, A. A. Stark, C. Tucker, K. Vanderlinde, J. D. Vieira, and R. Williamson. The 10 Meter South Pole Telescope. PASP, 123:568–581, May 2011. doi: 10.1086/659879.

R. A. C. Croft and C. A. Metzler. Weak-Lensing Surveys and the Intrinsic Correlation of Galaxy Ellipticities. ApJ, 545:561–571, December 2000. doi: 10.1086/317856.

S. Das, B. D. Sherwin, P. Aguirre, J. W. Appel, J. R. Bond, C. S. Carvalho, M. J. Devlin, J. Dunkley, R. Dünner, T. Essinger-Hileman, J. W. Fowler, A. Hajian, M. Halpern, M. Hasselfield, A. D. Hincks, R. Hlozek, K. M. Huffenberger, J. P. Hughes, K. D. Irwin, J. Klein, A. Kosowsky, R. H. Lupton, T. A. Marriage, D. Marsden, F. Menanteau, K. Moodley, M. D. Niemack, M. R. Nolta, L. A. Page, L. Parker, E. D. Reese, B. L. Schmitt, N. Sehgal, J. Sievers, D. N. Spergel, S. T. Staggs, D. S. Swetz, E. R. Switzer,

R. Thornton, K. Visnjic, and E. Wollack. Detection of the Power Spectrum of Cosmic Microwave Background Lensing by the Atacama Cosmology Telescope. Physical Review Letters, 107(2):021301, July 2011. doi: 10.1103/PhysRevLett.107.021301.

S. Dodelson. Modern cosmology. Academic Press, 2003.

S. Dodelson. CMB-cluster lensing. Phys. Rev. D, 70(2):023009, July 2004a. doi: 10.1103/PhysRevD.70.023009.

S. Dodelson. Cluster masses: Accounting for structure along the line of sight. Phys. Rev. D, 70(2):023008, July 2004b. doi: 10.1103/PhysRevD.70.023008.

S. Dodelson and G. D. Starkman. Galaxy-CMB Lensing. ArXiv Astrophysics e-prints, May 2003.

A. R. Duffy, J. Schaye, S. T. Kay, and C. Dalla Vecchia. Dark matter halo concentrations in the Wilkinson Microwave Anisotropy Probe year 5 cosmology. MNRAS, 390:L64–L68, October 2008. doi: 10.1111/j.1745-3933.2008.00537.x.

A. R. Duffy, J. Schaye, S. T. Kay, C. Dalla Vecchia, R. A. Battye, and C. M. Booth. Impact of baryon physics on dark matter structures: a detailed simulation study of halo density profiles. MNRAS, 405:2161–2178, July 2010. doi: 10.1111/j.1365-2966.2010.16613.x.

J. Dunkley, R. Hlozek, J. Sievers, V. Acquaviva, P. A. R. Ade, P. Aguirre, M. Amiri, J. W. Appel, L. F. Barrientos, E. S. Battistelli, J. R. Bond, B. Brown, B. Burger, J. Chervenak, S. Das, M. J. Devlin, S. R. Dicker, W. Bertrand Doriese, R. Dünner, T. Essinger-Hileman, R. P. Fisher, J. W. Fowler, A. Hajian, M. Halpern, M. Hasselfield, C. Hernández-Monteagudo, G. C. Hilton, M. Hilton, A. D. Hincks, K. M. Huffenberger, D. H. Hughes, J. P. Hughes, L. Infante, K. D. Irwin, J. B. Juin, M. Kaul, J. Klein, A. Kosowsky, J. M. Lau, M. Limon, Y.-T. Lin, R. H. Lupton, T. A. Marriage, D. Marsden, P. Mauskopf, F. Menanteau, K. Moodley, H. Moseley, C. B. Netterfield, M. D. Niemack, M. R. Nolta,

L. A. Page, L. Parker, B. Partridge, B. Reid, N. Sehgal, B. Sherwin, D. N. Spergel, S. T. Staggs, D. S. Swetz, E. R. Switzer, R. Thornton, H. Trac, C. Tucker, R. Warne, E. Wollack, and Y. Zhao. The Atacama Cosmology Telescope: Cosmological Parameters from the 2008 Power Spectrum. ApJ, 739:52, September 2011. doi: 10.1088/0004-637X/739/1/52.

E. George et al. in prep. . 2014.

O. Y. Gnedin, A. V. Kravtsov, A. A. Klypin, and D. Nagai. Response of Dark Matter Halos to Condensation of Baryons: Cosmological Simulations and Improved Adiabatic Contraction Model. ApJ, 616:16–26, November 2004. doi: 10.1086/424914.

O. Y. Gnedin, D. Ceverino, N. Y. Gnedin, A. A. Klypin, A. V. Kravtsov, R. Levine, D. Nagai, and G. Yepes. Halo Contraction Effect in Hydrodynamic Simulations of Galaxy Formation. ArXiv e-prints, August 2011.

A. H. Guth. Inflationary universe: A possible solution to the horizon and flatness problems. Phys. Rev. D, 23:347–356, January 1981. doi: 10.1103/PhysRevD.23.347.

N. Hand, G. E. Addison, E. Aubourg, N. Battaglia, E. S. Battistelli, D. Bizyaev, J. R. Bond, H. Brewington, J. Brinkmann, B. R. Brown, S. Das, K. S. Dawson, M. J. Devlin, J. Dunkley, R. Dunner, D. J. Eisenstein, J. W. Fowler, M. B. Gralla, A. Hajian, M. Halpern, M. Hilton, A. D. Hincks, R. Hlozek, J. P. Hughes, L. Infante, K. D. Irwin, A. Kosowsky, Y.-T. Lin, E. Malanushenko, V. Malanushenko, T. A. Marriage, D. Marsden, F. Menanteau, K. Moodley, M. D. Niemack, M. R. Nolta, D. Oravetz, L. A. Page, N. Palanque-Delabrouille, K. Pan, E. D. Reese, D. J. Schlegel, D. P. Schneider, N. Sehgal, A. Shelden, J. Sievers, C. Sifón, A. Simmons, S. Snedden, D. N. Spergel, S. T. Staggs, D. S. Swetz, E. R. Switzer, H. Trac, B. A. Weaver, E. J. Wollack, C. Yeche, and C. Zunckel. Evidence of Galaxy Cluster Motions with the Kinematic Sunyaev-Zel'dovich Effect. Physical Review Letters, 109(4):041101, July 2012. doi: 10.1103/PhysRevLett.109.041101.

Y. Hezaveh, K. Vanderlinde, G. Holder, and T. de Haan. Lensing Noise in Millimeter-wave Galaxy Cluster Surveys. ApJ, 772:121, August 2013. doi: 10.1088/0004-637X/772/2/121.

G. Hinshaw, D. Larson, E. Komatsu, D. N. Spergel, C. L. Bennett, J. Dunkley, M. R. Nolta, M. Halpern, R. S. Hill, N. Odegard, L. Page, K. M. Smith, J. L. Weiland, B. Gold, N. Jarosik, A. Kogut, M. Limon, S. S. Meyer, G. S. Tucker, E. Wollack, and E. L. Wright. Nine-year Wilkinson Microwave Anisotropy Probe (WMAP) Observations: Cosmological Parameter Results. ApJS, 208:19, October 2013. doi: 10.1088/0067-0049/208/2/19.

H. Hoekstra. How well can we determine cluster mass profiles from weak lensing? MNRAS, 339:1155–1162, March 2003. doi: 10.1046/j.1365-8711.2003.06264.x.

H. Hoekstra and B. Jain. Weak Gravitational Lensing and Its Cosmological Applications. Annual Review of Nuclear and Particle Science, 58:99–123, November 2008. doi: 10.1146/annurev.nucl.58.110707.171151.

H. Hoekstra, J. Hartlap, S. Hilbert, and E. van Uitert. Effects of distant large-scale structure on the precision of weak lensing mass measurements. MNRAS, 412:2095–2103, April 2011. doi: 10.1111/j.1365-2966.2010.18053.x.

G. Holder and A. Kosowsky. Gravitational Lensing of the Microwave Background by Galaxy Clusters. ApJ, 616:8–15, November 2004. doi: 10.1086/424808.

W. Hu. Mapping the Dark Matter through the Cosmic Microwave Background Damping Tail. ApJ, 557:L79–L83, August 2001. doi: 10.1086/323253.

W. Hu and T. Okamoto. Mass Reconstruction with Cosmic Microwave Background Polarization. ApJ, 574:566–574, August 2002. doi: 10.1086/341110.

W. Hu, S. DeDeo, and C. Vale. Cluster mass estimators from CMB temperature and polarization lensing. New Journal of Physics, 9:441, December 2007a. doi: 10.1088/1367-2630/9/12/441.

W. Hu, D. E. Holz, and C. Vale. CMB cluster lensing: Cosmography with the longest lever arm. Phys. Rev. D, 76(12):127301, December 2007b. doi: 10.1103/PhysRevD.76.127301.

D. Huterer, D. Kirkby, R. Bean, A. Connolly, K. Dawson, S. Dodelson, A. Evrard, B. Jain, M. Jarvis, E. Linder, R. Mandelbaum, M. May, A. Raccanelli, B. Reid, E. Rozo, F. Schmidt, N. Sehgal, A. Slosar, A. van Engelen, H.-Y. Wu, and G. Zhao. Growth of Cosmic Structure: Probing Dark Energy Beyond Expansion. ArXiv e-prints, September 2013.

N. Itoh, Y. Kohyama, and S. Nozawa. Relativistic Corrections to the Sunyaev-Zeldovich Effect for Clusters of Galaxies. ApJ, 502:7–15, July 1998. doi: 10.1086/305876.

Y. P. Jing and Y. Suto. Triaxial Modeling of Halo Density Profiles with High-Resolution N-Body Simulations. ApJ, 574:538–553, August 2002. doi: 10.1086/341065.

M. Kaplinghat, L. Knox, and Y.-S. Song. Determining Neutrino Mass from the Cosmic Microwave Background Alone. Physical Review Letters, 91(24):241301, December 2003. doi: 10.1103/PhysRevLett.91.241301.

R. Keisler, C. L. Reichardt, K. A. Aird, B. A. Benson, L. E. Bleem, J. E. Carlstrom, C. L. Chang, H. M. Cho, T. M. Crawford, A. T. Crites, T. de Haan, M. A. Dobbs, J. Dudley, E. M. George, N. W. Halverson, G. P. Holder, W. L. Holzapfel, S. Hoover, Z. Hou, J. D. Hrubes, M. Joy, L. Knox, A. T. Lee, E. M. Leitch, M. Lueker, D. Luong-Van, J. J. McMahon, J. Mehl, S. S. Meyer, M. Millea, J. J. Mohr, T. E. Montroy, T. Natoli, S. Padin, T. Plagge, C. Pryke, J. E. Ruhl, K. K. Schaffer, L. Shaw, E. Shirokoff, H. G. Spieler, Z. Staniszewski, A. A. Stark, K. Story, A. van Engelen, K. Vanderlinde, J. D. Vieira, R. Williamson, and O. Zahn. A Measurement of the Damping Tail of the Cosmic Microwave Background Power Spectrum with the South Pole Telescope. ApJ, 743:28, December 2011. doi: 10.1088/0004-637X/743/1/28.

K. Koyama and R. Maartens. Structure formation in the Dvali Gabadadze Porrati cosmo-

logical model. J. Cosmology Astropart. Phys., 1:016, January 2006. doi: 10.1088/1475-7516/2006/01/016.

G. P. Lepage. A New Algorithm for Adaptive Multidimensional Integration. Journal of Computational Physics, 27:192, May 1978. doi: 10.1016/0021-9991(78)90004-9.

A. Lewis and A. Challinor. Weak gravitational lensing of the CMB. Phys. Rep., 429:1–65, June 2006. doi: 10.1016/j.physrep.2006.03.002.

A. Lewis and L. King. Cluster masses from CMB and galaxy weak lensing. Phys. Rev. D, 73(6):063006, March 2006. doi: 10.1103/PhysRevD.73.063006.

A. D. Linde. A new inflationary universe scenario: A possible solution of the horizon, flatness, homogeneity, isotropy and primordial monopole problems. Physics Letters B, 108:389–393, February 1982. doi: 10.1016/0370-2693(82)91219-9.

Z. Ma, W. Hu, and D. Huterer. Effects of Photometric Redshift Uncertainties on Weak-Lensing Tomography. ApJ, 636:21–29, January 2006. doi: 10.1086/497068.

D. Merritt, A. W. Graham, B. Moore, J. Diemand, and B. Terzić. Empirical Models for Dark Matter Halos. I. Nonparametric Construction of Density Profiles and Comparison with Parametric Models. AJ, 132:2685–2700, December 2006. doi: 10.1086/508988.

C. A. Metzler, M. White, and C. Loken. The Effect of the Cosmic Web on Cluster Weak Lensing Mass Estimates. ApJ, 547:560–573, February 2001. doi: 10.1086/318406.

M. Millea, O. Doré, J. Dudley, G. Holder, L. Knox, L. Shaw, Y.-S. Song, and O. Zahn. Modeling Extragalactic Foregrounds and Secondaries for Unbiased Estimation of Cosmological Parameters from Primary Cosmic Microwave Background Anisotropy. ApJ, 746:4, February 2012. doi: 10.1088/0004-637X/746/1/4.

L. M. Mocanu, T. M. Crawford, J. D. Vieira, K. A. Aird, M. Aravena, J. E. Austermann, B. A. Benson, M. Béthermin, L. E. Bleem, M. Bothwell, J. E. Carlstrom, C. L. Chang,

S. Chapman, H.-M. Cho, A. T. Crites, T. de Haan, M. A. Dobbs, W. B. Everett, E. M. George, N. W. Halverson, N. Harrington, Y. Hezaveh, G. P. Holder, W. L. Holzapfel, S. Hoover, J. D. Hrubes, R. Keisler, L. Knox, A. T. Lee, E. M. Leitch, M. Lueker, D. Luong-Van, D. P. Marrone, J. J. McMahon, J. Mehl, S. S. Meyer, J. J. Mohr, T. E. Montroy, T. Natoli, S. Padin, T. Plagge, C. Pryke, A. Rest, C. L. Reichardt, J. E. Ruhl, J. T. Sayre, K. K. Schaffer, E. Shirokoff, H. G. Spieler, J. S. Spilker, B. Stalder, Z. Staniszewski, A. A. Stark, K. T. Story, E. R. Switzer, K. Vanderlinde, and R. Williamson. Extragalactic Millimeter-wave Point-source Catalog, Number Counts and Statistics from 771 deg^2 of the SPT-SZ Survey. ApJ, 779:61, December 2013. doi: 10.1088/0004-637X/779/1/61.

S. Naess, M. Hasselfield, J. McMahon, M. D. Niemack, G. E. Addison, P. A. R. Ade, R. Allison, M. Amiri, A. Baker, N. Battaglia, J. A. Beall, F. de Bernardis, J. Bond, J. Britton, E. Calabrese, H.-m. Cho, K. Coughlin, D. Crichton, S. Das, R. Datta, M. J. Devlin, S. R. Dicker, J. Dunkley, R. Dünner, J. W. Fowler, A. E. Fox, P. Gallardo, E. Grace, M. Gralla, A. Hajian, M. Halpern, S. Henderson, J. C. Hill, G. C. Hilton, M. Hilton, A. D. Hincks, R. Hlozek, P. Ho, J. Hubmayr, K. M. Huffenberger, J. P. Hughes, L. Infante, K. Irwin, R. Jackson, J. Klein, B. Koopman, A. Kosowsky, D. Li, T. Louis, M. Lungu, M. Madhavacheril, T. A. Marriage, L. Maurin, F. Menanteau, K. Moodley, C. Munson, L. Newburgh, J. Nibarger, M. R. Nolta, L. A. Page, C. Pappas, B. Partridge, F. Rojas, B. Schmitt, N. Sehgal, B. D. Sherwin, J. Sievers, S. Simon, D. N. Spergel, S. T. Staggs, E. R. Switzer, R. Thornton, H. Trac, C. Tucker, A. Van Engelen, J. Ward, and E. J. Wollack. The Atacama Cosmology Telescope: CMB Polarization at $200 < l < 9000$. ArXiv e-prints, May 2014.

D. Nagai, A. V. Kravtsov, and A. Vikhlinin. Effects of Galaxy Formation on Thermodynamics of the Intracluster Medium. ApJ, 668:1–14, October 2007. doi: 10.1086/521328.

J. F. Navarro, C. S. Frenk, and S. D. M. White. The Structure of Cold Dark Matter Halos. ApJ, 462:563, May 1996. doi: 10.1086/177173.

J. F. Navarro, A. Ludlow, V. Springel, J. Wang, M. Vogelsberger, S. D. M. White, A. Jenkins, C. S. Frenk, and A. Helmi. The diversity and similarity of simulated cold dark matter haloes. MNRAS, 402:21–34, February 2010. doi: 10.1111/j.1365-2966.2009.15878.x.

A. B. Newman, T. Treu, R. S. Ellis, D. J. Sand, C. Nipoti, J. Richard, and E. Jullo. The Density Profiles of Massive, Relaxed Galaxy Clusters. I. The Total Density Over Three Decades in Radius. ApJ, 765:24, March 2013. doi: 10.1088/0004-637X/765/1/24.

S. Padin, Z. Staniszewski, R. Keisler, M. Joy, A. A. Stark, P. A. R. Ade, K. A. Aird, B. A. Benson, L. E. Bleem, J. E. Carlstrom, C. L. Chang, T. M. Crawford, A. T. Crites, M. A. Dobbs, N. W. Halverson, S. Heimsath, R. E. Hills, W. L. Holzapfel, C. Lawrie, A. T. Lee, E. M. Leitch, J. Leong, W. Lu, M. Lueker, J. J. McMahon, S. S. Meyer, J. J. Mohr, T. E. Montroy, T. Plagge, C. Pryke, J. E. Ruhl, K. K. Schaffer, E. Shirokoff, H. G. Spieler, and J. D. Vieira. South Pole Telescope optics. Appl. Opt., 47:4418–4428, August 2008. doi: 10.1364/AO.47.004418.

T. Plagge, B. A. Benson, P. A. R. Ade, K. A. Aird, L. E. Bleem, J. E. Carlstrom, C. L. Chang, H.-M. Cho, T. M. Crawford, A. T. Crites, T. de Haan, M. A. Dobbs, E. M. George, N. R. Hall, N. W. Halverson, G. P. Holder, W. L. Holzapfel, J. D. Hrubes, M. Joy, R. Keisler, L. Knox, A. T. Lee, E. M. Leitch, M. Lueker, D. Marrone, J. J. McMahon, J. Mehl, S. S. Meyer, J. J. Mohr, T. E. Montroy, S. Padin, C. Pryke, C. L. Reichardt, J. E. Ruhl, K. K. Schaffer, L. Shaw, E. Shirokoff, H. G. Spieler, B. Stalder, Z. Staniszewski, A. A. Stark, K. Vanderlinde, J. D. Vieira, R. Williamson, and O. Zahn. Sunyaev-Zel'dovich Cluster Profiles Measured with the South Pole Telescope. ApJ, 716:1118–1135, June 2010. doi: 10.1088/0004-637X/716/2/1118.

Planck Collaboration, P. A. R. Ade, N. Aghanim, C. Armitage-Caplan, M. Arnaud, M. Ashdown, F. Atrio-Barandela, J. Aumont, C. Baccigalupi, A. J. Banday, and et al. Planck 2013 Results. XXIV. Constraints on primordial non-Gaussianity. ArXiv e-prints, March 2013.

Planck collaboration, P. A. R. Ade, N. Aghanim, C. Armitage-Caplan, M. Arnaud, M. Ashdown, F. Atrio-Barandela, J. Aumont, C. Baccigalupi, A. J. Banday, and et al. Planck 2013 results. XV. CMB power spectra and likelihood. ArXiv e-prints, March 2013.

Planck Collaboration, P. A. R. Ade, N. Aghanim, C. Armitage-Caplan, M. Arnaud, M. Ashdown, F. Atrio-Barandela, J. Aumont, C. Baccigalupi, A. J. Banday, and et al. Planck 2013 results. XVI. Cosmological parameters. ArXiv e-prints, March 2013a.

Planck Collaboration, P. A. R. Ade, N. Aghanim, C. Armitage-Caplan, M. Arnaud, M. Ashdown, F. Atrio-Barandela, J. Aumont, C. Baccigalupi, A. J. Banday, and et al. Planck 2013 results. XX. Cosmology from Sunyaev-Zeldovich cluster counts. ArXiv e-prints, March 2013b.

Planck Collaboration, P. A. R. Ade, N. Aghanim, C. Armitage-Caplan, M. Arnaud, M. Ashdown, F. Atrio-Barandela, J. Aumont, C. Baccigalupi, A. J. Banday, and et al. Planck 2013 results. XVII. Gravitational lensing by large-scale structure. ArXiv e-prints, March 2013c.

E. Rozo, R. H. Wechsler, E. S. Rykoff, J. T. Annis, M. R. Becker, A. E. Evrard, J. A. Frieman, S. M. Hansen, J. Hao, D. E. Johnston, B. P. Koester, T. A. McKay, E. S. Sheldon, and D. H. Weinberg. Cosmological Constraints from the Sloan Digital Sky Survey maxBCG Cluster Catalog. ApJ, 708:645–660, January 2010. doi: 10.1088/0004-637X/708/1/645.

J. Ruhl, P. A. R. Ade, J. E. Carlstrom, H.-M. Cho, T. Crawford, M. Dobbs, C. H. Greer, N. w. Halverson, W. L. Holzapfel, T. M. Lanting, A. T. Lee, E. M. Leitch, J. Leong, W. Lu, M. Lueker, J. Mehl, S. S. Meyer, J. J. Mohr, S. Padin, T. Plagge, C. Pryke, M. C. Runyan, D. Schwan, M. K. Sharp, H. Spieler, Z. Staniszewski, and A. A. Stark. The South Pole Telescope. In C. M. Bradford, P. A. R. Ade, J. E. Aguirre, J. J. Bock, M. Dragovan, L. Duband, L. Earle, J. Glenn, H. Matsuhara, B. J. Naylor, H. T. Nguyen, M. Yun, and J. Zmuidzinas, editors, Z-Spec: a broadband millimeter-wave grating

spectrometer: design, construction, and first cryogenic measurements, volume 5498 of Society of Photo-Optical Instrumentation Engineers (SPIE) Conference Series, pages 11–29, October 2004. doi: 10.1117/12.552473.

R. K. Sachs and A. M. Wolfe. Perturbations of a Cosmological Model and Angular Variations of the Microwave Background. ApJ, 147:73, January 1967. doi: 10.1086/148982.

S. J. Schmidt, B. Ménard, R. Scranton, C. B. Morrison, M. Rahman, and A. M. Hopkins. Inferring the Redshift Distribution of the Cosmic Infrared Background. ArXiv e-prints, June 2014.

U. Seljak and M. Zaldarriaga. Direct signature of an evolving gravitational potential from the cosmic microwave background. Phys. Rev. D, 60(4):043504, August 1999. doi: 10.1103/PhysRevD.60.043504.

U. Seljak and M. Zaldarriaga. Lensing-induced Cluster Signatures in the Cosmic Microwave Background. ApJ, 538:57–64, July 2000. doi: 10.1086/309098.

E. Shirokoff, C. L. Reichardt, L. Shaw, M. Millea, P. A. R. Ade, K. A. Aird, B. A. Benson, L. E. Bleem, J. E. Carlstrom, C. L. Chang, H. M. Cho, T. M. Crawford, A. T. Crites, T. de Haan, M. A. Dobbs, J. Dudley, E. M. George, N. W. Halverson, G. P. Holder, W. L. Holzapfel, J. D. Hrubes, M. Joy, R. Keisler, L. Knox, A. T. Lee, E. M. Leitch, M. Lueker, D. Luong-Van, J. J. McMahon, J. Mehl, S. S. Meyer, J. J. Mohr, T. E. Montroy, S. Padin, T. Plagge, C. Pryke, J. E. Ruhl, K. K. Schaffer, H. G. Spieler, Z. Staniszewski, A. A. Stark, K. Story, K. Vanderlinde, J. D. Vieira, R. Williamson, and O. Zahn. Improved Constraints on Cosmic Microwave Background Secondary Anisotropies from the Complete 2008 South Pole Telescope Data. ApJ, 736:61, July 2011. doi: 10.1088/0004-637X/736/1/61.

K. M. Smith, O. Zahn, and O. Doré. Detection of gravitational lensing in the cosmic microwave background. Phys. Rev. D, 76(4):043510, August 2007. doi: 10.1103/PhysRevD.76.043510.

Z. Staniszewski, P. A. R. Ade, K. A. Aird, B. A. Benson, L. E. Bleem, J. E. Carlstrom, C. L. Chang, H.-M. Cho, T. M. Crawford, A. T. Crites, T. de Haan, M. A. Dobbs, N. W. Halverson, G. P. Holder, W. L. Holzapfel, J. D. Hrubes, M. Joy, R. Keisler, T. M. Lanting, A. T. Lee, E. M. Leitch, A. Loehr, M. Lueker, J. J. McMahon, J. Mehl, S. S. Meyer, J. J. Mohr, T. E. Montroy, C.-C. Ngeow, S. Padin, T. Plagge, C. Pryke, C. L. Reichardt, J. E. Ruhl, K. K. Schaffer, L. Shaw, E. Shirokoff, H. G. Spieler, B. Stalder, A. A. Stark, K. Vanderlinde, J. D. Vieira, O. Zahn, and A. Zenteno. Galaxy Clusters Discovered with a Sunyaev-Zel'dovich Effect Survey. ApJ, 701:32–41, August 2009. doi: 10.1088/0004-637X/701/1/32.

R. A. Sunyaev and Y. B. Zeldovich. The Observations of Relic Radiation as a Test of the Nature of X-Ray Radiation from the Clusters of Galaxies. Comments on Astrophysics and Space Physics, 4:173, November 1972.

C. Vale, A. Amblard, and M. White. Cluster lensing of the CMB. New A, 10:1–15, November 2004. doi: 10.1016/j.newast.2004.04.003.

A. van Engelen, R. Keisler, O. Zahn, K. A. Aird, B. A. Benson, L. E. Bleem, J. E. Carlstrom, C. L. Chang, H. M. Cho, T. M. Crawford, A. T. Crites, T. de Haan, M. A. Dobbs, J. Dudley, E. M. George, N. W. Halverson, G. P. Holder, W. L. Holzapfel, S. Hoover, Z. Hou, J. D. Hrubes, M. Joy, L. Knox, A. T. Lee, E. M. Leitch, M. Lueker, D. Luong-Van, J. J. McMahon, J. Mehl, S. S. Meyer, M. Millea, J. J. Mohr, T. E. Montroy, T. Natoli, S. Padin, T. Plagge, C. Pryke, C. L. Reichardt, J. E. Ruhl, J. T. Sayre, K. K. Schaffer, L. Shaw, E. Shirokoff, H. G. Spieler, Z. Staniszewski, A. A. Stark, K. Story, K. Vanderlinde, J. D. Vieira, and R. Williamson. A Measurement of Gravitational Lensing of the Microwave Background Using South Pole Telescope Data. ApJ, 756:142, September 2012. doi: 10.1088/0004-637X/756/2/142.

A. van Engelen, S. Bhattacharya, N. Sehgal, G. P. Holder, O. Zahn, and D. Nagai. CMB

Lensing Power Spectrum Biases from Galaxies and Clusters Using High-angular Resolution Temperature Maps. ApJ, 786:13, May 2014. doi: 10.1088/0004-637X/786/1/13.